ChemCatChem

ChemCatChem
Chemistry Europe
European Chemical Societies Publishing

RESEARCH ARTICLE

Isopropanol Dehydration to Propylene: The Impact of Acid–Base Sites Strength, Dispersion and Nature

Tristan Cabanis[1] | Aline Auroux[1] | Jean-Luc Dubois[2] | Nicolas Sbirrazzuoli[3] | Georgeta Postole[1]

[1]Université Lyon 1, CNRS, IRCELYON, Villeurbanne, France | [2]Trinseo Netherlands B.V., Hoek, The Netherlands | [3]Institut De Chimie De Nice (ICN)–UMR CNRS 7272, Université Côte d'Azur (UCA), Nice, France

Correspondence: Nicolas Sbirrazzuoli (nicolas.sbirrazzuoli@univ-cotedazur.fr) | Georgeta Postole (georgeta.postole@ircelyon.univ-lyon1.fr)

Received: 14 January 2026 | **Revised:** 19 March 2026 | **Accepted:** 19 March 2026

Keywords: acid–base properties | adsorption/reaction calorimetry | isopropanol dehydration | kinetics

ABSTRACT

Three bulk oxides were studied to elucidate the dependence of the surface mechanism involved in the dehydration of isopropanol to propylene. Niobium oxide (acid), magnesium oxide (basic) and alumina (amphoteric) were selected for this study due to their distinct acid–base properties. The complementarity of infrared and microcalorimetry methods was used to accurately correlate surface properties with catalytic activity. The latter were evidenced using a reactor inside a microcalorimeter linked to gas chromatography and subsequent kinetic computations. Acid sites are essential for isopropanol to coordinatively adsorb and initiate a surface reaction under catalytic conditions. A solely basic surface exhibits isopropanol physical adsorption under continuous inert flow, with no surface reaction. The presence of both acidic and basic sites allows for easier dissociation of the alcohol. The synergetic effect of acid–base pairs on isopropanol adsorption and conversion is confirmed by the study of amorphous silica–alumina. Surface hydroxyls are also involved in the adsorption. The effective activation energy determined by advanced kinetic computations suggests a first order mechanism on acidic surfaces. On the amphoteric solid, the results suggest the presence of both second order and first-order elimination mechanism. The water produced during the reaction shown to alter the surface properties and reaction pathway. These results highlight the important role of acid–base site strength, nature and distribution and their synergetic effect on reaction mechanisms.

1 | Introduction

Propylene (PEN) is a key compound in the petrochemical industry and a fundamental molecule in the production of plastics and chemicals. The global demand for propylene exceeds 100 million tonnes annually, with a growth rate of 4%/year [1]. To meet this demand, global production capacity is expected to reach 200 tonnes by 2030 [2]. Today, propylene is mainly obtained as a co-product of hydrocarbon steam cracking or catalytic cracking for ethylene production but this hydrocarbon dependency does not allow to fully meet the growing demand [3–6]. Furthermore, the decline in fossil resources and their negative impact of their use on the environment call for clean processes for propylene production, which account for low carbon emissions and improved energy efficiency [1, 6].

The dehydration of isopropanol (IPA) is a promising alternative route for more sustainable and closed-loop processes for propylene synthesis [7, 8]. Isopropanol production via acetone hydrogenation is indeed very promising, as acetone is primarily a co-product of phenol in the cumene oxidation process [9]. The market gap between these two chemicals has widened considerably due to the shift from acetone to ethylene as a feedstock for methyl methacrylate production [10–12]. Additionally, the cumene process uses propylene as a starting reactant. Hydrogenation of acetone into isopropanol, followed by the

latter's dehydration into propylene, enables carbon recycling.The catalytic conversion of isopropanol is a well-known reaction often used to evaluate the acid–base properties of the catalyst's surface at a laboratory scale. Acid sites trigger dehydration to either propylene or diisopropyl ether, while basic sites contribute to the dehydrogenation reaction to acetone [13–15]. It is worth mentioning that dehydrogenation takes place under certain conditions, the presence of redox properties or high temperatures [16–18]. While usual acid–base characterisation methods, such as Hammett titration [19] infrared spectroscopy [20, 21], adsorption microcalorimetry [22, 23], solid-state nuclear magnetic resonance [24] and temperature programmed desorption [25, 26], allow to clearly identify the nature, strength and distribution of active sites, it is difficult to establish an absolute correlation with catalytic properties. These characterisations use different probe molecules or conditions far from usual catalytic reactions and do not account for the dynamic conditions in heterogenous catalysis. Test reactions, including isopropanol conversion, bridge this gap and provide interesting tools for acid–base characterisation [16, 27]. Although isopropanol conversion is widely used as a test reaction in laboratories, the surface mechanisms of isopropanol dehydration to propylene are still discussed [28–30]. Few systematic comparative studies exist between acidic, basic and amphoteric catalysts for isopropanol dehydration and a detailed understanding of catalytic activities as a function of defined acid–base properties of the active sites has drawn our attention.

The objective of this study is to compare the behaviour of three bulk oxides to elucidate the dependence of the surface mechanisms involved in the catalytic process (i.e., adsorption, reaction and desorption) on the acid–base characteristics of the catalyst. Niobium oxide, magnesium oxide and alumina were selected for this study due to their distinct acid–base properties, namely, solely acidic, solely basic and amphoteric, respectively. This high contrast makes it possible to isolate the influence of site nature and strength on each step of the catalytic process, that is, adsorption, reaction and desorption. Amphoteric silica–alumina was investigated for comparison and validation. In this study, data from static and dynamic measurements enabled to accurately correlate surface properties with catalytic activity. The complementary nature of infrared and microcalorimetric methods using different probe molecules is used to determine the surface properties and behaviour of the catalysts. Combining in situ measurements of adsorption and reaction/desorption heats with the kinetic computation of calorimetric signals [31], allowed to improve the comprehension of fundamental surface mechanisms of acid–base reactions and provided perspectives on catalyst design for sustainable propylene production.

2 | Experimental Section

2.1 | Catalysts

The studied catalysts are commercially available materials with different acid–base properties: alumina (Al_2O_3) from BASF, niobium oxide (Nb_2O_5) from H.C. Starck and magnesium oxide (MgO) from Sigma-Aldrich. Alumina was provided in extruded form. The catalyst was therefore ground in an agate mortar and sieved according to technical requirements. Niobium oxide and magnesium oxide were provided in powder form. In this case, when the particle size was below technical requirements, the powder was initially compressed into pellets using a hydraulic press at a pressure of 5 tons. The pellets were then ground and sieved to obtain the desired particle size. Amphoteric silica–alumina (SiO_2-Al_2O_3) from Sasol Germany GmbH (Brunsbüttel, Germany) with a $SiO_2/(SiO_2+Al_2O_3)$ ratio of 30% was also investigated for comparison.

2.2 | X-Ray Diffraction

The x-ray diffraction (XRD) patterns of the commercial powders were recorded on a Brüker D8 Advance powder diffractometer with monochromatic copper Kα radiation of 1.5406 Å wavelength, equipped with a 1-D fast multistrip detector (LynxEye, 192 channels, 2.95°) and a nickel filter. The diffractograms, registered within the 2θ range from 4° to 80° with a 0.02° step size, were analysed using the Diffract Eva software and the powder diffraction file (PDF) 5+ database.

2.3 | Brunauer–Emmett–Teller, Nitrogen Sorption Isotherm

Nitrogen (N_2) sorption isotherms were recorded at −196°C on an ASAP 2010 or TriStar II Plus (Micromeritics) apparatus. The sample was first outgassed under a secondary vacuum for 3 h at 300°C. The apparent specific surface area (S_{BET}) was derived from the Brunauer–Emmett–Teller (BET) standard equation. The interval of relative pressure used to linearize the BET model equation was $0.005 \leq P/P_0 \leq 0.10$ with at least 5 points used to obtain a correlation coefficient > 0.999. The total pore volume (V_{pore}) was calculated at $P/P_0 = 0.95$ on the adsorption branch. The mesopore size distribution was determined by analysing the adsorption branch of the N_2 adsorption/desorption isotherm via the Barrett, Joyner and Halenda (BJH) method.

2.4 | Acid–Base Adsorption Microcalorimetry

The acid–base properties were determined at 150°C by adsorption microcalorimetry of ammonia (NH_3) and sulphur dioxide (SO_2) probe molecules, respectively. The adsorption experiments were performed in a heat flow microcalorimeter (Tian-Calvet type, C80 from Setaram) linked to a conventional volumetric apparatus and equipped with a Barocel capacitance manometer (datametrics) for pressure measurements. Prior to the ammonia or sulphur dioxide adsorption, about 100 mg of the sample was treated overnight at 400°C (1°C min^{-1}) under vacuum. The differential heats of adsorption were measured as a function of coverage by repeatedly sending small doses of probe molecules over the powder until an equilibrium pressure of about 67 Pa was reached. The sample was then outgassed for 30 min at the same temperature, and a second adsorption was performed (still at 150°C) until an equilibrium pressure of about 27 Pa was attained to calculate the amount of irreversible adsorption at this pressure. The difference between the amounts of gas adsorbed at 27 Pa during the two adsorption runs corresponds to the number of strong adsorption sites. Further information and calculations are available in the Supporting Information.

2.5 | Fourier Transform Infrared Adsorption

Fourier transform infrared (FTIR) spectra were recorded at a resolution of 4 cm^{-1} in the region of 1000 to 4000 cm^{-1} by using a Thermo Scientific (Waltham, MA, USA) Nicolet 8700 Fourier transform spectrometer equipped with a deuterated L-alanine doped triglycine sulphate (DTGS) detector and OMNIC software. Prior to analysis, approximately 30 to 40 mg of sample was grounded in an agate mortar and pressed into self-supporting discs by applying a pressure of 5 tons. The self-supported wafer was placed into a cell with CaF_2 windows and pretreated under oxygen overnight at 400°C (1°C min^{-1}), followed by 2 h outgassing at the same temperature before adsorption. Then, the cell was cooled down to 23°C, and the sample was contacted with NH_3 (15 mbars) for 1 h before following the desorption of the adsorbed species, under vacuum, at the desired temperatures (100°C, 200°C and 300°C). The infrared (IR) spectra were recorded after each step: pretreatment, adsorption and desorption at these temperatures. Spectrum background was recorded using an empty cell.

2.6 | Pulse Catalytic Test Calorimetry

Pulse catalytic tests were carried out in a quartz microreactor placed in a differential scanning calorimeter (DSC) (CALVET PRO from Setaram) connected to a gas chromatograph (GC). A detailed description of the device is provided in a previous work [31].

Typically, 0.03 mL (i.e., 15 to 25 mg) of catalyst powder with particle size between 300 and 425 µm was loaded and constantly flushed with a helium flow of 30 mL min^{-1}. The pressure of 3 bars inside the measurement cell is imposed by the pressure drop of the chromatographic column.

At the inlet of the reactor, a 6-way valve, kept at 150°C, equipped with a calibrated injection loop of 500 µL is constantly refiled by a feed gas mixture of anhydrous isopropanol diluted in helium. Isopropanol is evaporated in a saturator set at 30.5°C and fed with a constant flow of helium (10 mL min^{-1}). Antoine's equation and ideal gas law are used to calculate the numbers of probe molecules or reagents in the calibrated loop. The amount of isopropanol per injection is then 1.15 µmol. The outlet of the reactor is directly connected to the chromatographic column (Prorapak Q at 150°C). A thermal conductivity detector (TCD) and a flame ionisation detector (FID) are placed in series at the column outlet. To prevent condensation, all lines connecting the saturator, the calorimeter and the chromatograph are heated at 110°C. For safety reasons, the isopropanol flask is regularly check for the presence of peroxides, and/or discharged and refilled.

As injections start, the 6-port valve is switched to direct the diluted probe molecules of the reagent to the microreactor. Calorimetric curves display the heat flow as a function of time, while FID chromatograms are used for quantification of the reagent and products. The TCD results are used to qualitatively observe water. A duration of 90 min is kept between each pulse to provide a complete return to the baseline for both the heat flow and the GC detector signals.

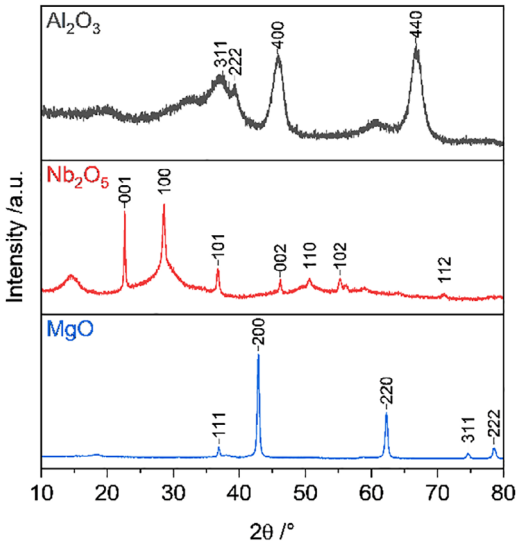

FIGURE 1 | XRD patterns of alumina (grey), niobium oxide (red) and magnesium oxide (blue).

2.7 | Signal Processing

To gain insight into the respective heats of adsorption and reaction/desorption, the calorimetric curves are deconvoluted using the Fraser-Suzuki function and the least squares method with a Python program. To conduct kinetic computations, the reaction rate and extent of conversion are determined from the deconvoluted calorimetric data and FID signals. The isoconversional Friedman and Vyazovkin's method [32–34] is then applied to the exothermic and endothermic contributions to calculate the effective activation energy (E_α) as a function of the extent of conversion (α). The isoconversional method is based on the statement that, at a defined extent of conversion, the activation energy is only a function of temperature. Therefore, no reaction model is needed. The variation of the effective activation energy as a function of the extent of conversion indicates the complexity of the reaction mechanism, that is, if the latter consists of one or more steps. The variation also provides hints about the nature of the limiting steps during the process. This method has been successfully applied to several physicochemical transformations and heterogeneous catalytic reactions [31, 32, 35–37]. Further information and calculations are available in the Supporting Information.

3 | Results and Discussion

3.1 | Structural and Textural Properties

Figure 1 displays the XRD patterns of the studied catalysts. The alumina XRD pattern (2θ = 37.6°, 39.5°, 45.8° and 66.8°), showing a small degree of crystallinity, corresponds to the pure cubic crystal system (PDF-00-001-1303) commonly known as the gamma phase. The peak positions of niobium oxide diffractogram (2θ = 22.6°, 28.6°, 36.7°, 46.2°, 50.7°, 55.2°, 56.1°, 59.0° and 71.0°) reveal a hexagonal crystal system (PDF-00-007-0061). Finally, the magnesium oxide XRD pattern (2θ = 36.9°, 24.9°, 62.2°, 74.6° and 78.5°) corresponds to the cubic crystal system (PDF-01-71-1176) of the well-crystallized phase [38].

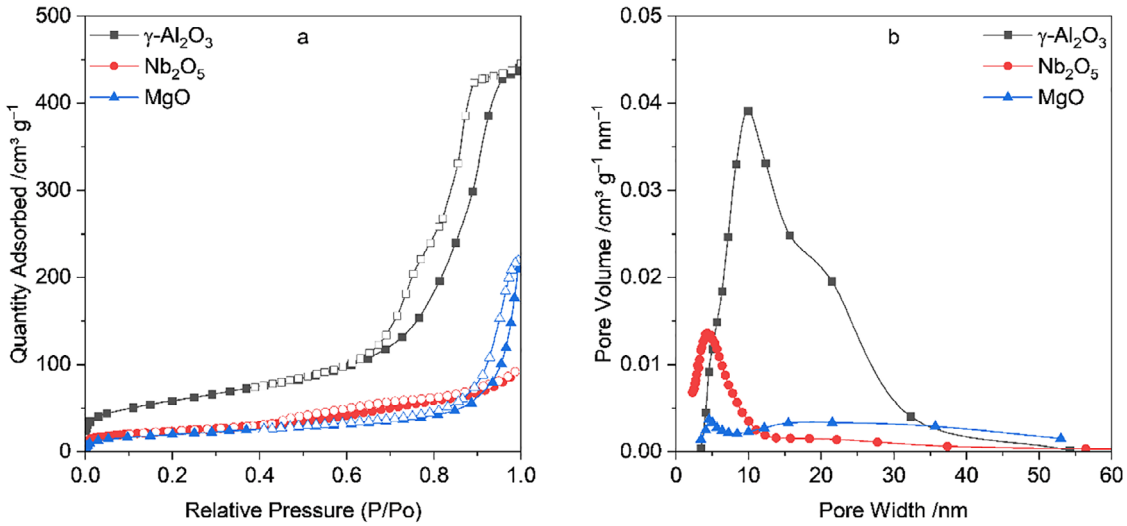

FIGURE 2 | (a) Nitrogen adsorption (filled) and desorption (empty) isotherms and (b) pore size distributions obtained through the BJH method of alumina (square, grey), niobium oxide (circle, red) and magnesium oxide (triangle, blue).

TABLE 1 | Textural properties of gamma alumina, niobium oxide and magnesium oxide.

Catalysts	S_{BET}/m² g⁻¹	V_{porous}/cm³ g⁻¹	V_{meso}/cm³ g⁻¹	$D_p^{average}$/nm[a]	D_p^{peak}/nm
Al_2O_3	208	0.69	0.68 (≈ 98%)	13.3	9.9
Nb_2O_5	83	0.12	0.12 (100%)	5.7	4.3
MgO	71	0.34	0.31 (≈ 92%)	20.0	na

[a] $D_p^{average} = \frac{4V_{porous}}{S_{BET}}$.

Figure 2 displays the nitrogen adsorption–desorption isotherms (Figure 2a) and pore size distributions (Figure 2b) of the three oxides. The textural properties of the solids are summarised in Table 1. All samples show a type IV isotherm (IUPAC classification) [39, 40] with a hysteresis loop characteristic of mesoporous structure [41, 42]. Alumina, with the highest adsorption at low relative pressures (< 0.06), shows some residual microporosity, while MgO is characterised by a low degree of micropores. The classification of De Boer and Lippens [43, 44]. (Type A, B, C, D or E) and the UPAC classification [39, 40]. (H1, H2, H3 or H4) can be used to describe the hysteresis loop. For a clearer view of the hysteresis loops, Figures S5–S7 show the independent nitrogen sorption curves.

Figure 2a shows that alumina presents an almost vertical N_2 uptake starting at a relative pressure of 0.65. On the desorption branch, the presence of two capillary condensation steps from relative pressures of 0.65 to 0.80 and from 0.80 to 0.96 indicates a bimodal pore distribution for Al_2O_3 [45]. Type B (H2) hysteresis is associated with wide pores with short openings or pores formed by parallel plates with some distance between each other. The bimodal distribution is clearly visible in Figure 2b as alumina displays a maximum pore volume at 9.9 nm with a clear shoulder at 21.5 nm for an average pore size of 13.3 nm.

Niobium oxide displays a slopping adsorption branch. The desorption branch shows a well-defined condensation step from relative pressure of 0.45 to 0.80, following a less intense step from 0.80 to 1.00. This hysteresis is a combination of type B (H2) with pronounced type E characteristics and is associated with pores with ink-bottle shapes, that is, a wide body and a narrow neck. The pore size distribution shows a well-defined peak maximum of 4.3 nm. A significant pore volume remains for pore width above 12 nm, which explains the slightly higher value of the average pore size of 5.7 nm. These observations are in line with the corresponding hysteresis.

Magnesium oxide is characterised by a vertical adsorption branch starting at a relative pressure of 0.85 and a desorption branch with two condensation steps (at relative pressure between 0.41 and 0.75; 0.75 and 1.00). Therefore, MgO shows a Type A hysteresis loop (H1) corresponding to tubular pores with open ends. The two condensation steps, however, underline some narrower parts. The large average pore diameter of 20.0 nm combined with one well-defined peak at a pore width of 4.5 nm, confirmed previous statements.

FTIR was used to give insights into the nature of groups and species on the fresh catalyst surfaces. Figure 3 shows the feature of the three oxides calcined at 400°C.

In the stretching region, adsorption bands observed between 3800 and 3500 cm^{-1} are associated to the stretching of the surface hydroxyl groups present on each catalyst. Multiple studies have already been conducted regarding the surface hydroxyls of the three studied catalysts [46–51]. In the deformation region, alumina shows weak adsorption bands at 1563 and 1477 cm^{-1} while magnesium oxide shows intense peaks at 1568, 1509 and

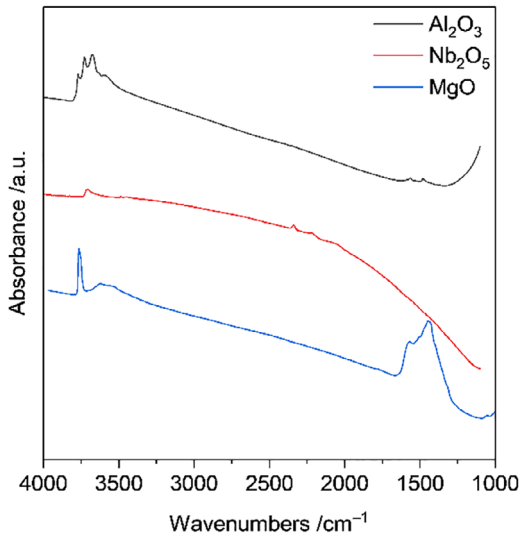

FIGURE 3 | Infrared spectra of alumina (grey), niobium oxide (red) and magnesium oxide (blue).

1447 cm^{-1}. These adsorptions correspond to strongly adsorbed residual carbonates [52–55].

Niobium oxide exhibits small adsorption bands at 2335, 2211 and 2056 cm^{-1} which should correspond to strongly bonded carbon dioxide, nitrile and alkynes probably derived from the synthesis or the industrial treatment process resulting in some contamination of the commercial sample. Further CHNS analyses were performed on fresh niobium oxide as displayed in Table S1 to confirm the presence of some nitrogen and carbon on the catalyst. Parts of these adsorbed species appear resistant to pretreatment under oxygen at 400°C [56].

3.2 | Acid–Base Site Properties

The acid–base properties of the catalysts studied are determined by adsorption microcalorimetry and infrared spectroscopy. These characterisations will make it possible to relate the acid–base properties to the catalytic properties in the next paragraphs.

3.2.1 | Strength and Distribution of Sites

In the following paragraphs, to compare surface properties, the adsorbed quantities of probe molecules are expressed in mol m^{-2}. The surface used here refers to the specific surface area (S_{BET}) obtained from nitrogen sorption experiments as presented in Table 1 and normalised using the catalyst mass loaded before adsorption.

Figure 4 displays the differential heats of adsorption of ammonia and sulphur dioxide on the studied catalysts as a function of the amount adsorbed. The proton affinities of ammonia and sulphur dioxide are 854 and 672 kJ mol^{-1}, respectively [57]. Since the adsorption strength depends on the proton affinity of the used probe, these values should be considered when comparing the results.

The initial differential heats of NH_3 adsorption on the clean surface of the catalyst, that is, the first injection, are − 185, − 166 and − 68 kJ mol^{-1} for alumina, niobium oxide and magnesium oxide, respectively. Then, the heat decreases almost linearly with the adsorbed amounts. Finally, the evolved heats reach very low values after uptakes of 1.68, 2.10 and 1.08 μmol m^{-2} for Al_2O_3, Nb_2O_5 and MgO, respectively. The linear decrease of the adsorption heats versus coverage and the important NH_3 uptake reflect the wide heterogenous distribution of alumina and niobium oxide surface sites strength. Available metal atoms on the surface, with different coordination degrees, that is, the number of oxygen atoms bonded to the cation, provides wide distribution of Lewis acid sites [20, 52]. Alumina displays higher adsorption heats of ammonia than niobium oxide when the uptake amount is below 0.68 μmol m^{-2}. Apart from the coordination and nature of the metallic atom, the stronger adsorption strength can be explained by the presence of various hydroxyl groups close to the Lewis acid sites on the catalyst surface. Hydroxyl groups can form hydrogen bonds with ammonia, increasing the adsorption strength [19]. Above 0.68 μmol m^{-2}, niobium oxide shows a stronger interaction with NH_3 and higher overall uptake (2.00 μmol m^{-2}) than Al_2O_3. The strength distribution of acid sites remains comparable for these two catalysts. In comparison, magnesium oxide, exhibiting significantly lower adsorption heats and a total NH_3 uptake of only 1.08 mol m^{-2}, shows very weak and very few acid sites. Surface carbonates, as display by FTIR on clean MgO surface explains this residual acidity.

Alumina shows a typical amphoteric character, with comparable amount and strength of acidic and basic sites (Figure 4). The heats of SO_2 adsorption (Figure 4b) show, after a first decrease from − 205 to − 173 kJ mol^{-1} at low coverage (up to 0.28 μmol m^{-2}), a noticeable plateau up to 0.66 μmol m^{-2} uptake. This may correspond to heats released during SO_2 adsorption on the predominant surface basic sites. Above, the heats of adsorption drop to low values after 1.82 μmol m^{-2} coverage. Niobium oxide is characterised by low number of basic sites (0.15 μmol m^{-2}) and low values of SO_2 adsorption heats which drops fast from − 113 to − 50 kJ mol^{-1}. Nb_2O_5 shows predominant acidic character. The SO_2 adsorption heats versus coverage display, for magnesium oxide, 2 plateaus at − 187 kJ mol^{-1}, up to 1.41 μmol m^{-2} uptake and − 165 kJ mol^{-1} between 1.97 and 2.54 μmol m^{-2} uptake, respectively. The presence of these plateaus indicates a fairly homogeneous distribution of basic sites. The sharp drop of differential heats to 24 kJ mol^{-1}, after a total uptake of 4.26 μmol m^{-2}, accounts for the saturation of the chemisorption sites. MgO shows a predominant basic character with only a limited number of acid sites of weak strength.

Table 2 summarises the total ammonia and sulphur dioxide uptakes at 67 Pa (0.5 torr). This amount was used to determine the ratio of occupied surfaces, representing the percentage of the catalyst surface occupied by molecules adsorbed, as follows (Equation 1):

$$S_i^{occ} = \frac{\pi {d_i}^2 n_i^{ads} N_A}{4} \quad (1)$$

with S_i^{occ}, the ratio of occupied surface (m^2%) d_i, the kinetic diameter of molecule i (m) n_i^{ads}, the adsorbed quantity of molecules i (mol m^{-2}) and N_A, the Avogadro constant (mol^{-1}).

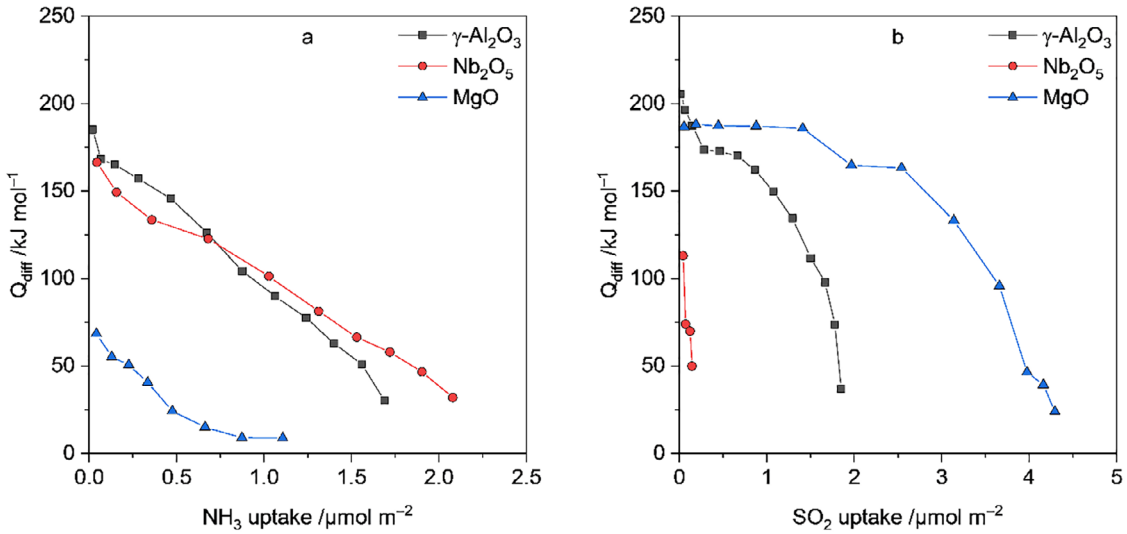

FIGURE 4 | Differential heats of adsorption of (a) ammonia and (b) sulphur dioxide on alumina (square, grey), niobium oxide (circle, red) and magnesium oxide (triangle, blue) at 150°C.

TABLE 2 | Ammonia and sulphur dioxide uptakes and the corresponding occupied surface calculated from adsorption isotherms on the studied catalysts under an equilibrium pressure of 67 Pa.

Catalysts	NH_3 uptake/μmol m^{-2}	SO_2 uptake/μmol m^{-2}	NH_3 occupied surface[a]/%	SO_2 occupied surface[b]/%
Al_2O_3	1.67	1.82	8.43	13.25
Nb_2O_5	2.10	0.10	10.58	0.72
MgO	1.08	4.26	5.42	31.03

[a]With $d_{NH_3} = 3.26$ Å.
[b]With $d_{SO_2} = 3.90$ Å [58].

This acid–base surface study provides a better understanding of isopropanol's reactivity. Both acidic and basic surface sites are assumed to adsorb isopropanol as alcohols are indeed amphoteric molecules capable of both receiving and donating protons [59].

3.2.2 | Nature of Sites

To gain insight into the acid sites nature, static infrared adsorption of ammonia on the studied catalysts was performed. Figures 5–7 display the spectra of adsorbed ammonia as a function of the desorption temperature on alumina, niobium oxide and magnesium oxide, respectively. All spectra shown are subtracted by that of the corresponding catalyst presented in Figure 3. The raw spectra are available in Figures S8–S10.

When visible, the adsorption bands between 3400 and 3200 cm^{-1} are attributed to NH stretching vibrations, while bands between 1700 and 1470 cm^{-1} are attributed to the fundamental NH_2 or NH_3 deformation [61–63]. Our analyses focus on frequencies between 3800 and 3400 cm^{-1}, associated with surface hydroxyls, and between 1400 and 1000 cm^{-1}, associated with Brønsted and Lewis acid sites.

For Al_2O_3 (Figure 5a), the subtracted spectra in the stretching domain at 23°C show negative bands at 3770, 3758, 3726, 3669 and 3631 cm^{-1}. The disappearance of surface hydroxyl groups suggests the formation of hydrogen bonds between adsorbed ammonia and surface hydroxides. The large band visible at 3535 cm^{-1} is attributed to these new hydrogen bonds [63]. At higher temperatures, the negative bands disappear, but interestingly, the presence of a positive adsorption band at 3742 cm^{-1} at 200°C indicates the formation of a surface hydroxyl not present on the pretreated alumina. At this temperature, the cleavage of a N—H bond in ammonia can allow the formation of a new hydroxyl group [61]. In the bending domain, ammonia adsorbed on alumina provides adsorption bands at 1690, 1618, 1501, 1472, 1395, 1288, 1255 and 1204 cm^{-1} at 23°C. The bands observed from 1690, to 1472 cm^{-1} are attributed to the fundamental N-H_2 or N-H_3 deformation. The weak band at 1395 cm^{-1}, attributed to NH_4^+ species, indicates the presence of some Brønsted acid sites [63]. This band remains present up to a desorption temperature of 200°C, and accounts for the relatively important strength of these sites despite their low abundance. The three bands at 1288, 1255 and 1204 cm^{-1} are assigned to coordinated ammonia to Lewis's acid sites [62]. When temperature increases, one band disappears, while the other two are shifted to 1303 and 1278 cm^{-1} frequencies and remain present even at 300°C. The presence of different bands, stable at given temperatures, and their respective shifts suggest multiple Lewis's acid sites nature in agreement with the heterogeneity of acid sites observed by NH_3 adsorption microcalorimetry [64].

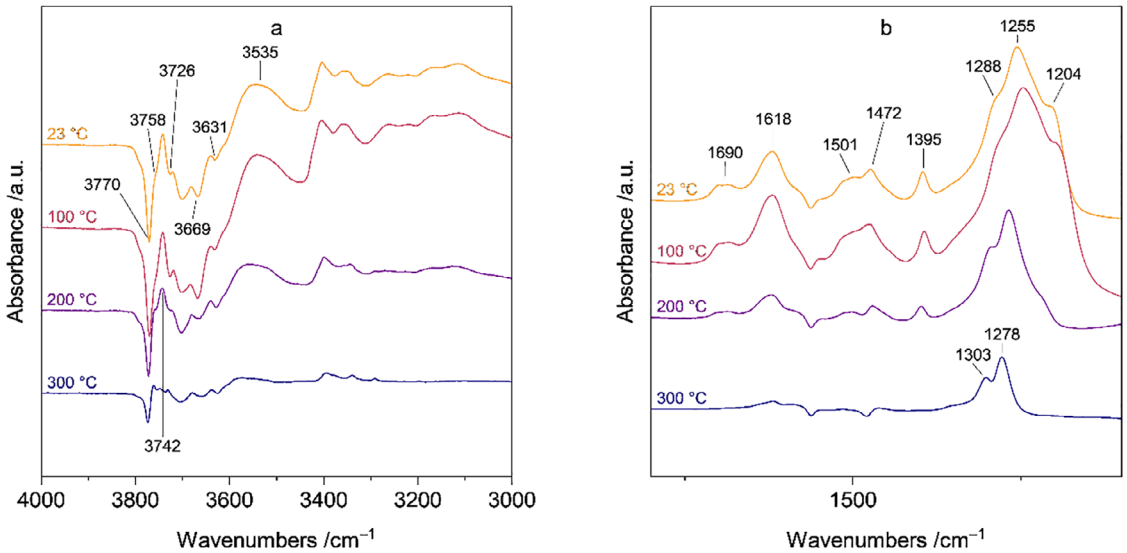

FIGURE 5 | Subtracted spectra in (a) the stretching and (b) the bending regions [60] obtained after ammonia adsorption as a function of temperature on alumina.

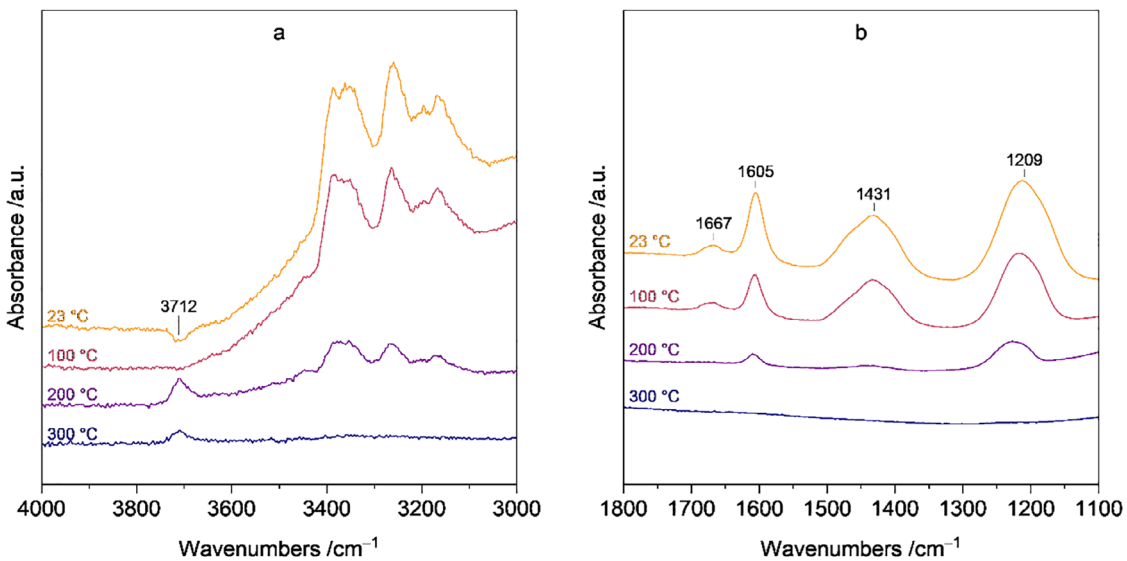

FIGURE 6 | Subtracted spectra in (a) the stretching and (b) the bending regions obtained after ammonia adsorption as a function of temperature on niobium oxide.

On niobium oxide (Figure 6), in the stretching region, the feature linked to hydroxyl groups (3710 cm^{-1}) first decreases at 23°C, before increasing with the temperature rise at 100°C and 200°C. The band finally decreases from 300°C before its disappearance at 400°C. Like for alumina, the adsorbed ammonia seems to be able to increase the number of hydroxyl groups by the dissociation of one N—H bond in the temperature range of 100°C to 200°C on niobium oxide. This hypothesis is supported by the presence of the band related to N-H_2 bending at 1605 cm^{-1} [65]. In the bending domain, the bands at 1431 and 1209 cm^{-1} are attributed to NH_4^+, that is, Brønsted acid sites, and coordinated ammonia, that is, Lewis's acid sites, respectively. Both sites exhibit a dramatic band decrease intensity at 200°C, before disappearing at 300°C.

Compared to alumina and niobium oxide, the adsorption of ammonia on magnesium oxide shows some very weak adsorption of ammonia and barely visible adsorption bands can be differentiated from the baseline (Figure 7). It is possible to distinguish, in the substituted spectra, the disappearance of the band at 3760 cm^{-1} corresponding to surface hydroxyls in the stretching region. The large band centred at 3557 cm^{-1} is attributed to hydrogen bonds between hydroxyls or surface oxygens and ammonia. In the bending region, the adsorption band at 1482 cm^{-1} is attributed to the asymmetric deformation of NH_3. The adsorption bands observable at 1380 and 1167 cm^{-1} are attributed to the symmetric deformation of NH_3 coordinated to a Lewis acid site [66]. The negative band at 1593 cm^{-1} indicates that the surface carbonates play a role in ammonia adsorption.

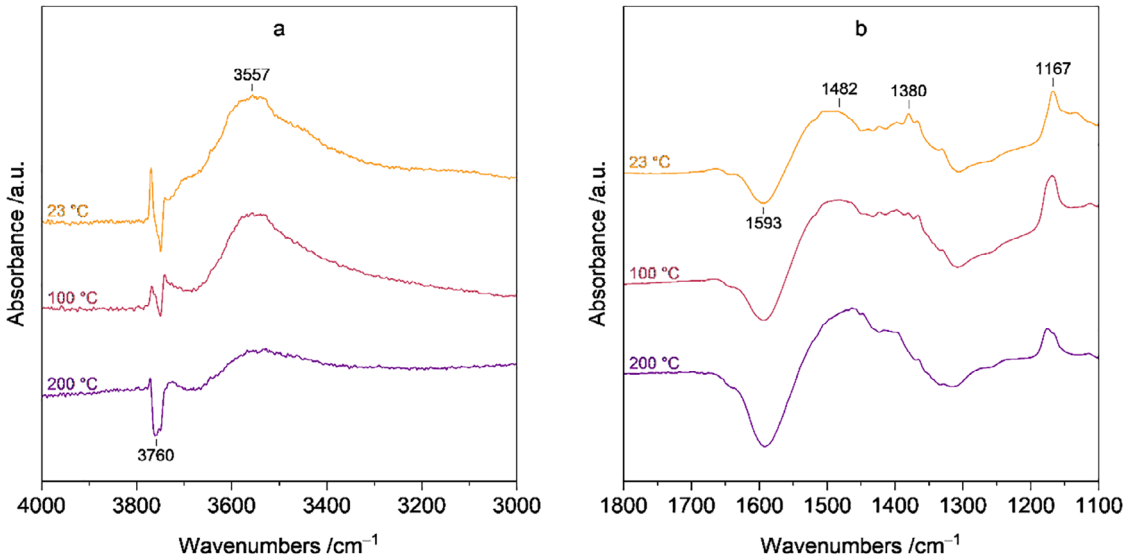

FIGURE 7 | Subtracted spectra in (a) the stretching and (b) the bending regions obtained after ammonia adsorption as a function of temperature on magnesium oxide.

These results support the almost complete absence of acidic sites on magnesium oxide and confirm that surface carbonates are the primary source of acidity.

It can be concluded that Lewis and Brønsted acid centres coexist on both alumina and niobium oxide. Magnesium oxide, on the other end, only displays a very limited amount of Lewis acid sites at studied temperatures. Based on the adsorption band intensities and NH_3 adsorption microcalorimetry, the Lewis sites of alumina appear to be the predominant type with a wide distribution, both in terms of strength and nature. Compared to alumina, niobium oxide displays important Brønsted sites, as evidenced by the relative intensity of the corresponding adsorption band. However, the Lewis sites of alumina can retain adsorbed ammonia at a temperature of 300°C, which is not the case with niobium oxide. Finally, the acidity of magnesium oxide is believed to be mainly due to surface carbonates.

In all three cases, the surface hydroxyl groups are very likely to play a role in the adsorption process by hydrogen bonding. This phenomenon is particularly visible on alumina, considering the range of possible and observable configurations of surface hydroxyls. Thus, the water produced by the reaction should have an impact on the catalytic activity and will be considered in the following paragraphs when catalytic activity and kinetics are studied.

3.3 | Isopropanol Adsorption

The isopropanol adsorption is the first step in the catalytic process. It is studied using static infrared spectroscopy and the pulse catalytic set up at low temperatures to provide only adsorption and desorption of the reagent.

3.3.1 | Mode of Isopropanol Adsorption

Knowing the types of acid sites present on our surfaces and to gain insight into the adsorption mode of the reactant, static infrared adsorptions were also performed with isopropanol as the probe molecule. Table 3 summarises the observed frequencies obtained with an empty cell loaded with 15 mbar of isopropanol. The spectrum is available in Figure S11.

TABLE 3 | Fundamental frequencies of gaseous isopropanol in an empty cell.

Assignments[a]	Wavenumbers/cm^{-1}
ν(O-H)	3660
ν(C-H3) a	2981 and 2971
ν(C-H3) s	2929
ν(C-H)	2889
δ(C-H3) a	1476 and 1462
δ(C-H3) s	1392 and 1384
δ(C-H), δ(O-H)	1263, 1251 and 1236
ν(C-C), ρ(C-H3)	1151 and 1073
δ(C-O)	965 and 953

[a]With ν stretching, δ scissoring, ρ rocking, *s* symmetric and *a* asymmetric.

Figures 8–10 display the subtracted spectra obtained after isopropanol adsorption as a function of the desorption temperature on alumina, niobium oxide and magnesium oxide, respectively. Corresponding raw spectra are available in Figures S12–S14.

On alumina at 75°C, the bands associated with surface hydroxyls disappear, while a large band at the lower wavenumbers of 3560 and 3516 cm^{-1} appears, corresponding to the formation of hydrogen-bonded surface hydroxyls (Figure 8a). When adsorbed, the three bands at 2980, 2971 and 2889 cm^{-1} observed in the gas phase are shifted to lower wavenumbers at 2964, 2933 and 2871 cm^{-1}, respectively. In the bending region, bands are observed at 1465 and 1377 cm^{-1} with shoulders at 1453 and 1338 cm^{-1}, respectively. These bands are attributed to the C-H_3 deformation

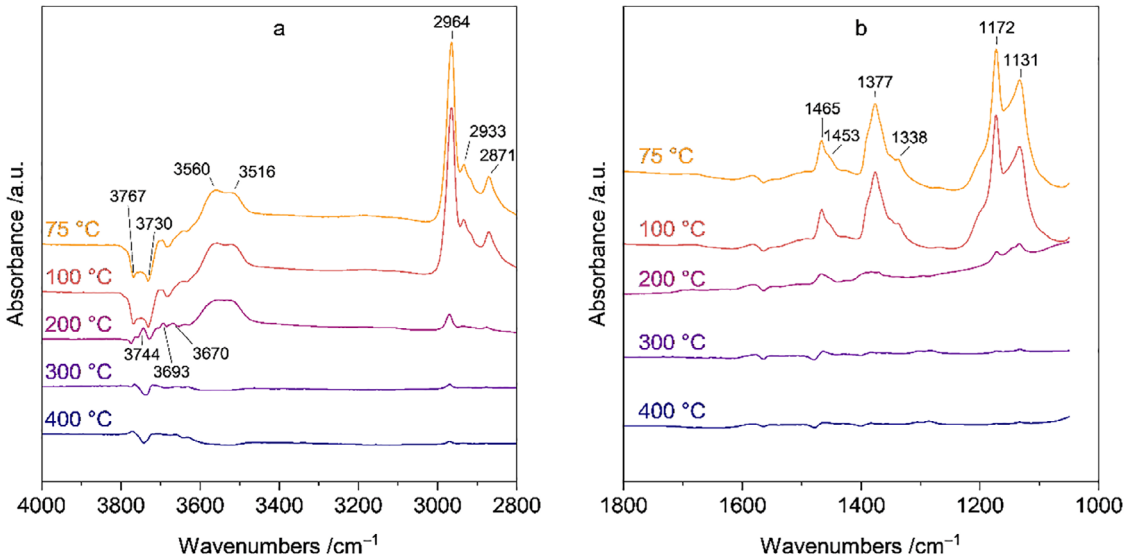

FIGURE 8 | Subtracted spectra in (a) the stretching and (b) the bending regions obtained after isopropanol adsorption as a function of temperature on alumina.

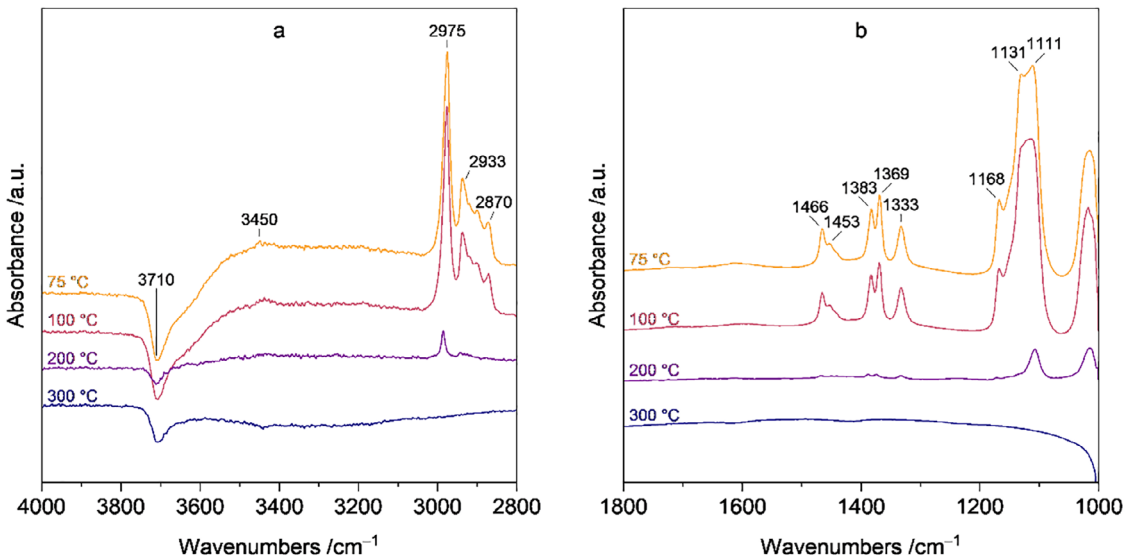

FIGURE 9 | Subtracted spectra in (a) the stretching and (b) the bending regions obtained after isopropanol adsorption as a function of temperature on niobium oxide.

previously observed in the gas phase at slightly higher frequencies. A weak, but visible band, initially not present in the gas phase, appears at 1337 cm^{-1} and is attributed to the vibrational coupling of C-H deformation. The triplet and the two bands attributed to δ(C-H), δ(O-H), ν(C-C) and ρ(C-H3) in the gas phase merge into two bands at 1172 and 1131 cm^{-1}. The disappearance of the O-H supports the formation of hydrogen bonds between the alcohol and the surface hydroxyls. The proximity of the obtained two bands with aluminium isopropoxide also suggests the presence of alkoxide species [67–69]. When the temperature increases, isopropanol remains adsorbed below 100°C. At 200°C, the intensity of all bands related to the fundamental stretching and deformation frequencies mostly disappeared. Interestingly, at 200°C, the formation of 3 new adsorption peaks at 3744, 3693 and 3670 cm^{-1} in the stretching region of surface hydroxyls is observed. Knowing that the dehydration of isopropanol to propylene on alumina can already take place at 125°C, part of isopropanol is probably desorbed as propylene. The water formed by the reaction remains adsorbed on the surface as hydroxyls and explains the presence of new surface hydroxyls compared to the clean, pretreated alumina. The absence of the adsorption band at 1635 cm^{-1}, typical of water bending mode [70, 71], indicates that only the water dissociated as hydroxyls remains stable under the experimental conditions. The absence of adsorption bands related to C=C or C(sp2)-H bonds evidences the absence of adsorbed propylene at 200°C and supports the idea that no strong interaction occurs between alkene and alumina at this temperature.

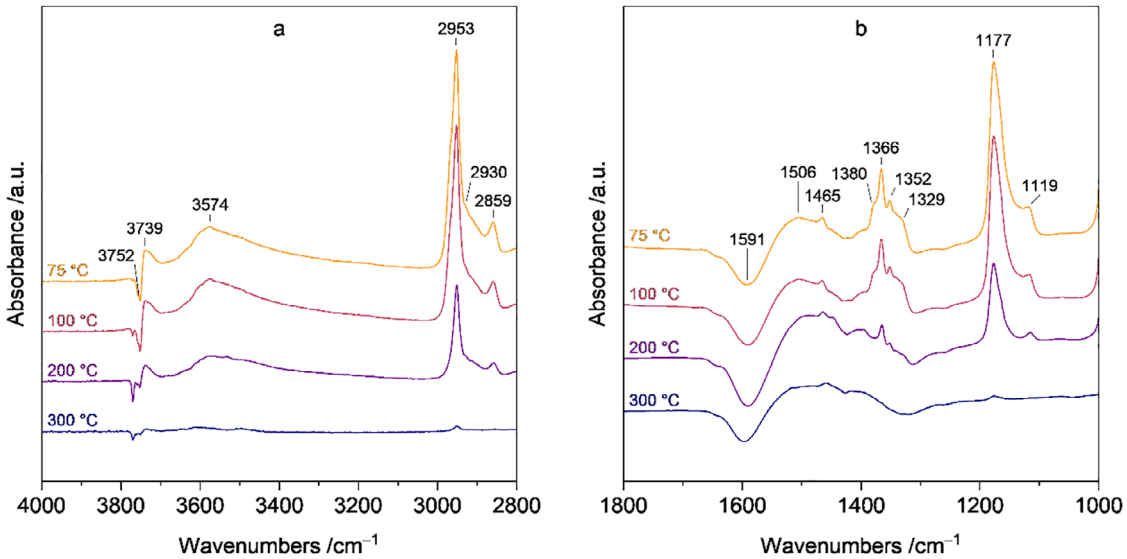

FIGURE 10 | Subtracted spectra in (a) the stretching and (b) the bending regions obtained after isopropanol adsorption as a function of temperature on magnesium oxide.

On niobium oxide at 75°C, the shift of the band at 3710 cm^{-1} associated with surface hydroxyl to a very large band centred at 3450 cm^{-1} in a lower frequency region suggests the formation of hydrogen bonds between the alcohol and the oxide (Figure 9). The three characteristic bands associated with C-H and C-H_3 stretching show, like in the case of alumina, a shift to lower wavenumbers of 2975, 2933 and 2870 cm^{-1}. The shifts look identical for both catalysts, except for the band associated with the asymmetric C-H_3 stretching (2981 cm^{-1} in the gas phase), which is less intense for niobium oxide. In the bending region, niobium oxide presents adsorption bands at 1466, 1453, 1383 and 1369 cm^{-1} associated with the asymmetric and symmetric C-H_3 bending. The intense band at 1333 cm^{-1}, previously observed as a weak band on alumina, shows a large enhancement due to the vibrational coupling of C-H deformation. The absence of the O-H deformation and the three bands at 1168, 1131 and 1111 cm^{-1} indicate the presence of coordinated species on Lewis's acid sites stabilised with hydrogen bonding.

On magnesium oxide (Figure 10), as with the two previously studied catalysts, a shift in the sharp band linked to the surface hydroxyls from 3752 cm^{-1} to a relatively sharp band at 3739 cm^{-1} and a large band centred at 3574 cm^{-1} provides evidence for the formation of hydrogen bonding between the surface and isopropanol molecules. It is interesting to note that the band of the lowest frequency is larger than that previously observed in the spectra of alumina and niobium oxide in the studied range of temperature. The presence of strong basic sites compared to other oxides would allow the formation of stronger hydrogen bonds between the surface basic sites and the alcohol. The stretching bands related to isopropanol C-H and C-H_3 groups are shifted to lowerwavenumbers of 2953, 2930 and 2859 cm^{-1}. It should be noted that this shift is more pronounced than that observed in the case of alumina and niobium oxide. In the bending region, negative and positive bands appear at 1591 and 1506 cm^{-1}, respectively. As previously observed during ammonia adsorption, these variations indicate the involvement of surface carbonates in adsorption. Adsorption bands at 1465, 1380, 1366 and 1352 cm^{-1} are associated with the asymmetric and symmetric CH_3 bending. Once more, a band related to the vibrational coupling of C-H deformation is observed at 1329 cm^{-1}. Its intensity is comparable to that observed with alumina. The bands at 1177 and 1119 cm^{-1} are associated with the coordinated species on Lewis's acid sites [47]. The increase in temperature has a significant impact on all bands corresponding to adsorbed isopropanol. However, the bands associated with surface carbonates do not show any significant variation and would underline some irreversible modifications of the surface carbonates.

As with ammonia adsorption, the importance of surface hydroxyls for alcohol adsorption is demonstrated by changes in the adsorption bands. The absence of the band associated with the (O-H) of gaseous isopropanol when adsorbed suggests that hydrogen bonding contributes to alcohol adsorption. In the bending region, all samples display the characteristic bands associated with coordinated alcohol. Interestingly, different shifts towards lower wavenumbers of the bands associated with ν(C-H_3) were observed between gaseous isopropanol and adsorbed isopropanol on the three studied catalysts. Displacement values of the ν(C-H_3) bands are 16, 6 and 28 cm^{-1} for alumina, niobium oxide and magnesium oxide, respectively. The acid–base properties of studied samples could explain this behaviour: the presence of basic O^{2-} surface sites can easily interact with hydrogen of the alcohol function, favouring the dissociation of alcohol in surface isopropoxide [72–74]. The resulting electronic delocalisation towards the CH_3 and CH groups weakens the C—H bonds. Isopropanol is thus believed to completely dissociate on magnesium oxide and undissociate on niobium oxide. Alumina, as an amphoteric catalyst, exhibits intermediate behaviour.

3.3.2 | Heat of Isopropanol Adsorption

In the pulse catalytic test set inside a calorimeter, the catalysts were saturated with adsorbed isopropanol at 75°C, where no reaction took place, by performing 16 injections. Only isopropanol was

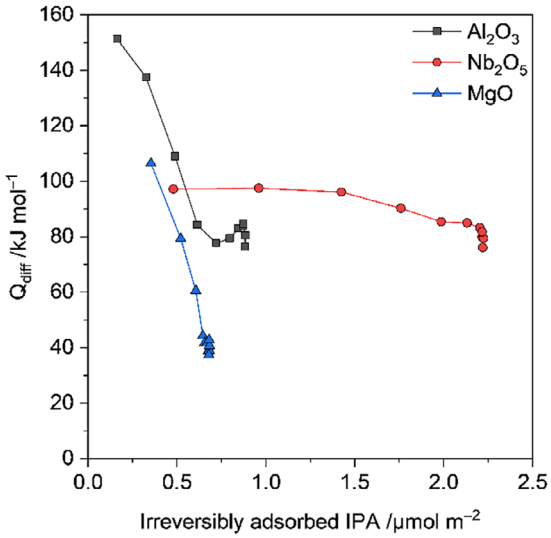

FIGURE 11 | Differential heats of adsorption as a function of the irreversibly adsorbed isopropanol for alumina (square, grey), niobium oxide (circle, red) and magnesium oxide (triangle, blue) at 75°C.

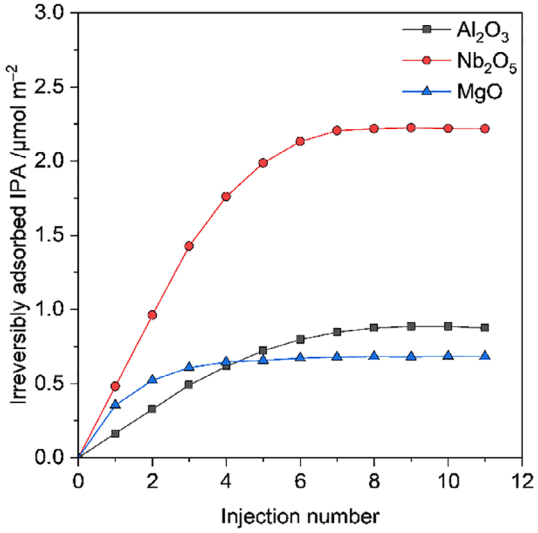

FIGURE 12 | Irreversible amounts of isopropanol adsorbed as a function of the injection number for alumina (square, grey), niobium oxide (circle, red) and magnesium oxide (triangle, blue) at 75°C.

observed by gas chromatography, meaning that only adsorption and desorption of the reactant occurred.

Figure 11 shows the differential heats of adsorption as a function of irreversibly adsorbed isopropanol.

All catalysts show a decrease in the differential heats of adsorption during the first injections, corresponding to the irreversible adsorption of isopropanol on strong sites of the surface. Then, a heat plateau is reached, corresponding to the reversible amounts of reactant under the 30 mL min^{-1} helium flow at 75°C. Alumina and magnesium oxide show relatively strong decreases from − 151 to − 84 kJ mol^{-1} after 1.53 µmol m^{-2} uptake and − 103 to − 44 kJ mol^{-1} after 2.09 µmol m^{-2} uptake during catalyst surface coverage, respectively. On the other end, niobium oxide exhibits a weak decrease in heat from − 97 to − 79 kJ mol^{-1} after 3.16 µmol m^{-2} uptake. At the plateau, gamma alumina, niobium oxide and magnesium oxide show reversible adsorption heats of 80, 79 and 37 kJ mol^{-1}, respectively. At high coverage, alumina and niobium oxide show identical differential heats of adsorption. The obtained values (− 80 and − 79 kJ mol^{-1}, respectively) are too high to consider only physical adsorption and seem close to the values observed when coordinative adsorption occurs between an oxide and an alcohol function [75]. The heats of adsorption obtained with magnesium oxide (− 38 kJ mol^{-1}) are close to the latent heat of condensation of isopropanol at 75°C (− 39.9 kJ mol^{-1} at 82°C) [76], meaning that only weak physical adsorption occurs on the catalyst surface and no further surface sites are available for chemical adsorption at 75°C.

At low coverage, the presence of basic sites results in strong irreversible adsorption on the fresh catalyst, as both alumina and magnesium oxide display a significant decrease in adsorption heat during the first pulses. This finding is consistent with previous infrared results and conclusions regarding the effect of basic sites on alcohol dissociation. It appears that the strongly and irreversibly adsorbed isopropanol exists in the form of dissociated alcohol. The acidic sites alone, as displayed by niobium oxide, give almost homogeneous adsorption strength and the absence of basicity does not allow alcohol dissociation. It follows that, at high coverage, acid sites provide a relatively strong reversible adsorption heat under helium flow (Figure 11). Figure 12 shows the irreversible amount of adsorbed isopropanol as a function of the injection number.

Gamma alumina, niobium oxide and magnesium oxide show irreversible amounts of 0.88, 2.22 and 0.68 µmol m^{-2} (182, 185 and 49 µmol g^{-1}), respectively. The isopropanol surface coverages, calculated using Equation (1) and the kinetic diameter of isopropanol (0.47 nm) [77], are 9.21%, 23.21% and 7.13% for Al_2O_3, Nb_2O_5 and MgO, respectively. Although experimental conditions, particularly temperature (75°C and 150°C for pulse and volumetric experiments, respectively), and the characteristics of the adsorbed molecules, in particular their proton affinity (793 and 854 kJ mol^{-1} for isopropanol and ammonia, respectively) [57], must be taken into consideration when comparing the pulse and volumetric experiments, it is possible to correlate the isopropanol adsorption results with the ammonia and sulphur dioxide data in Table 2. The catalysts capacity to irreversibly adsorb isopropanol appears to drastically increase with the total amount of acid sites.

The ratio of adsorbed isopropanol to ammonia (expressed in µmol m^{-2}) using the calorimetry-pulse experiment in comparison to the calorimetry-volumetry experiment can be determined. As stated above, the obtained ratios must be interpreted with care, since the temperature, which influences adsorption, differs between the compared experiments. Values of 0.52, 1.06 and 0.63 are obtained for alumina, niobium oxide and magnesium oxide, respectively. Since an ammonia molecule can only bind to one acidic site due to its single available electron pair, it is likely that some of the irreversibly adsorbed isopropanol, which has two available electron pairs in its alcohol function, is bound to multiple acid sites as bidental alkoxides on alumina and magnesium oxide. The 1:1 ratio in the case of niobium oxide supports the idea of monodental adsorption. This interpretation also supports the sudden decrease in adsorption heat for alumina and magnesium

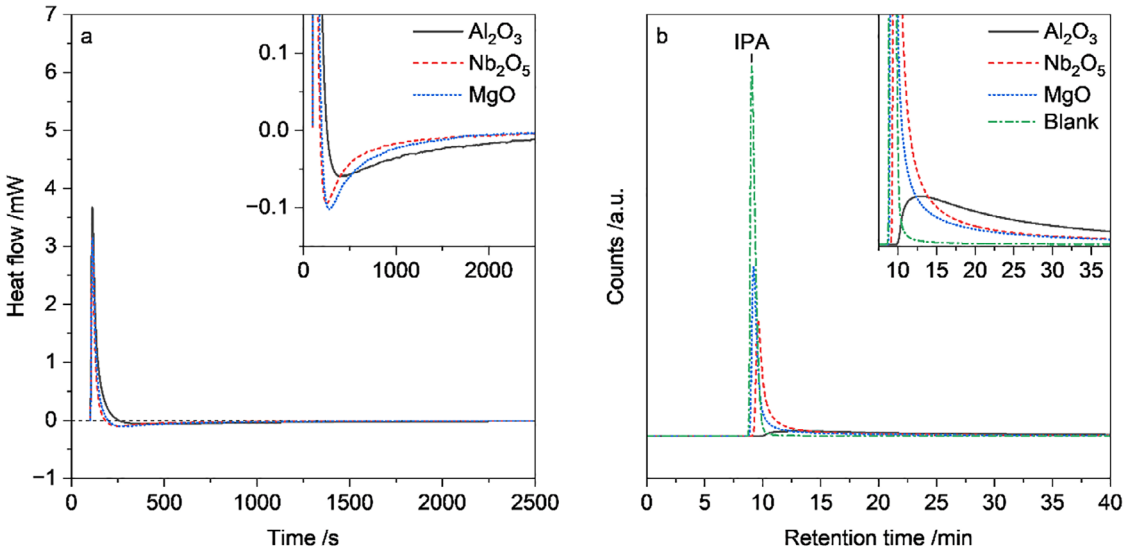

FIGURE 13 | Calorimetric (a) and FID (b) signals after a pulse of isopropanol when no further irreversible adsorption occurs, that is, injection number 16, on alumina (solid, black), niobium oxide (dash, red) and magnesium oxide (dot, blue) at 75°C. As a reference, FID signal obtained with an empty reactor is also displayed (dash and dot, green).

oxide compared to niobium oxide as well as infrared experiment conclusions: relatively high values during the first injections are explained by the strength of bidental and dissociated adsorption compared to monodental and undissociated adsorption. Figure 13 displays the calorimetric and FID signals obtained at 75°C after a pulse of isopropanol, when no further irreversible adsorption occurs.

In the case of alumina, the width of the endothermic peak in the calorimetric signal and the isopropanol peak in the FID signal are much greater than those observed in the case of niobium oxide and magnesium oxide. The average residence time of isopropanol in each catalyst can be estimated using the time difference between the exothermic and endothermic peak maximums. Values of 331, 142 and 168 s are obtained for alumina, niobium oxide and magnesium oxide, respectively. Residence time values can be correlated to the surface area of each sample. As alumina displays the most important BET surface area, it is highly probable that readsorption of the reagent takes place while crossing the catalytic bed, enhancing the residence time. Alumina shows a substantial mesopore volume, resulting in a mean residence time driven by intragranular diffusion. In contrast, the mesopore volumes of niobium oxide and magnesium oxide are significantly lower, and the mean residence time is only driven by intergranular diffusion.

3.4 | Catalytic Properties

The catalytic properties were evaluated in the pulse catalytic test right after the isopropanol adsorption experiment.

3.4.1 | Reaction at 175°C

To trigger the reaction, the temperature of the calorimeter from the pulse test was increased from 75°C to 300°C with 25°C steps. For each temperature, 5 injections were performed to ensure reproducibility. Figure 14 compares the calorimetric and FID signals obtained at 175°C for the 3 studied catalysts.

Both alumina and niobium oxide exhibit a complete conversion of isopropanol to propylene, while magnesium oxide does not show any conversion at 175°C. Although the basic properties of magnesium oxide are well defined, no acetone is produced at the low temperature of 175°C. This behaviour is explained by the absence of redox properties of MgO, which complements the basicity for dehydrogenation. Otherwise, acetone production requires temperatures above 300°C [16–18].

The calorimetric signals show a significant increase of the endothermic contribution for both alumina and niobium oxide. This is the expected behaviour, as the dehydration of isopropanol to propylene and water is an endothermic reaction (+ 52 kJ mol^{-1} at 175°C) [78]. The exothermic and endothermic contributions of the calorimetric signals are then deconvoluted using the Frazer–Suzuki equation [31]. The exothermic contribution is linked to the adsorption of isopropanol on the catalyst surface, while the endothermic heat is attributed to the reaction and desorption of products. Table 4 displays the in situ heats obtained at 175°C for alumina and niobium oxide.

The in situ heats of adsorption obtained after signal deconvolution are more important than those previously obtained at 75°C when maximum catalyst coverage was achieved. At low temperatures (75°C), the reagent can be adsorbed on all three types of sites: strong, medium and weak. However, at higher temperatures (175°C), adsorption occurs exclusively on the strong and medium sites. Additionally, development of new sites on the catalyst surface due to water formation is highly possible. The development of new sites is supported by the infrared adsorption experiment, which shows that new hydroxyl groups, believed to play an effective role in adsorption, are stable at defined temperatures.

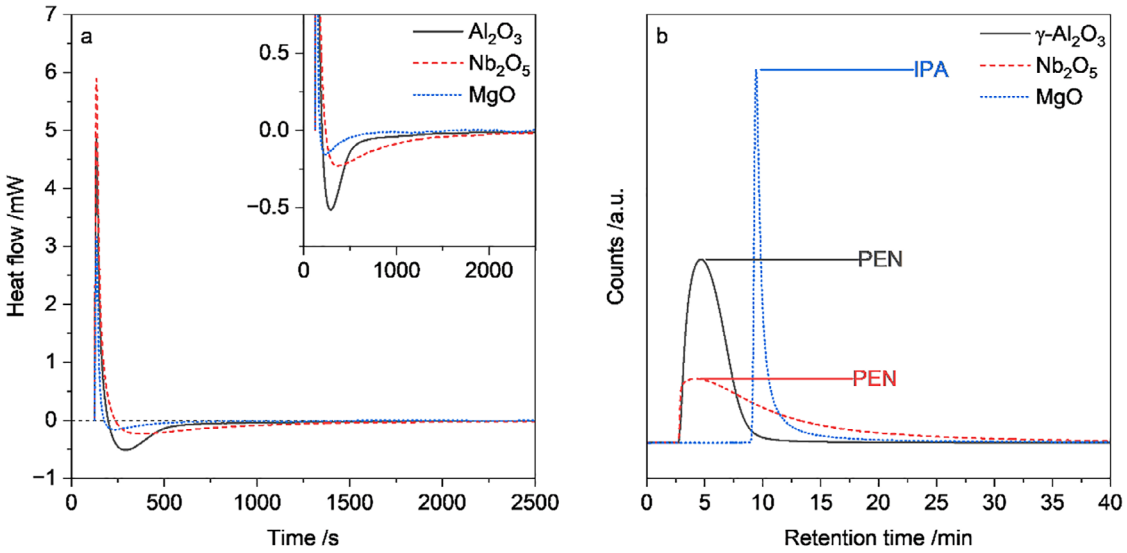

FIGURE 14 | Calorimetric (a) and FID (b) signals obtained after a pulse of isopropanol on alumina (solid, black), niobium oxide (dash, red) and magnesium oxide (dot, blue) at 175°C.

TABLE 4 | Heats of the exothermic and endothermic contributions at 175°C after 5 pulses.

Catalysts	Exothermic heat[a]/kJ mol^{-1}	Endothermic heat[b]/kJ mol^{-1}
Al_2O_3	−126	+134
Nb_2O_5	−136	+124

[a]Calculated using the amount of isopropanol adsorbed/reacted.
[b]Calculated using the amount of propylene produced.

Theoretically, the total heat, that is, the sum of adsorption and reaction/desorption heat, should be equal to the enthalpy of reaction under heterogenous conditions (i.e., + 52 kJ mol^{-1} at 175°C) when the conversion is total. In the present case, however, the sums of both contributions are + 8 and − 12 kJ mol^{-1} for alumina and niobium oxide, respectively. The presence of a supplementary exothermic reaction, such as coke or oligomer formation from the alcohol or the alkene, could explain this phenomenon. Considering the dimerization of propylene as a typical oligomerization reaction (−149 kJ mol^{-1} at 175°C) [78], a significant proportion of propylene should be converted to oligomers, explaining the heat differences. However, a carbon balance of 100% is reached for both catalysts and coke formation is more unlikely to occur under the studied temperatures. A very slow and undetectable desorption of water from active sites under the helium flow can most probably explain the differences observed. Water remains chemically adsorbed on the surface and argues for a strong exothermic interaction of water with the studied catalysts.

Alumina displays a complete conversion and selectivity towards propylene from 150°C to 300°C. Niobium oxide exhibits similar behaviour up to 200°C. From this temperature to 300°C, unidentified peaks appear on the chromatograms, indicating possible oligomerization reactions. Magnesium oxide starts displaying a propylene yield from 200°C, reaching 30%$_{PEN}$ at 300°C. An acetone peak is visible, but remains negligible from 225°C to 300°C.

3.4.2 | Advanced Kinetic Computations

To ensure reliable kinetic computations, a new set of experiments were performed at temperatures where significant variations in the shape of the endothermic calorimetric signal and propylene FID peak were observed. Figures 15–17 display the calorimetric signals and FID signals obtained after isopropanol injection at those relevant temperatures, that is, between 150°C and 175°C for alumina, between 175°C and 200°C for niobium oxide and 250 and 275°C for magnesium oxide. Steps of 5°C are applied to obtain 6 different temperatures. To ensure complete catalyst coverage and reproducibility between pulses, 10 injections were performed at the starting temperature, followed by 5 injections at the given incremental temperatures.

The significant variation in the shape of the calorimetric and FID signals observed as a function of temperature for alumina and niobium oxide confirm previous observations made when comparing catalysts at 175°C and underline the presence of two different kinetics. The important reduction in full width at half maximum for both the endothermic contribution in the calorimetric signal and the propylene peak in FID, following a 5°C temperature increase, indicates a phenomenon strongly influenced by temperature, that is, a thermally activated process such as a chemical reaction.

In contrast, magnesium oxide does not show a significant change in the shape of both endothermic and exothermic contributions in the overall temperature range. In the same way, the shape of the propylene peaks in the FID signals does not vary significantly compared to alumina and niobium oxide and remains sharp despite the temperature. The yield also remains relatively low, that is, from 1 to 3%$_{PEN}$ between 250°C and 275°C. Acetone is present only in small amounts as displayed in Figure S15 with

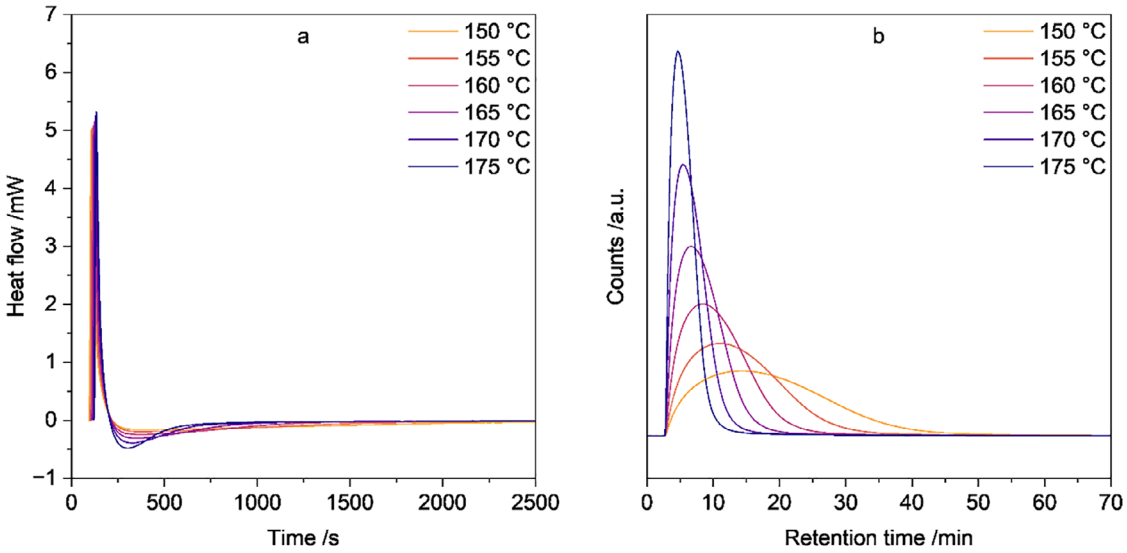

FIGURE 15 | Calorimetric (a) and FID (b) signals as a function of temperature obtained after isopropanol injection on alumina.

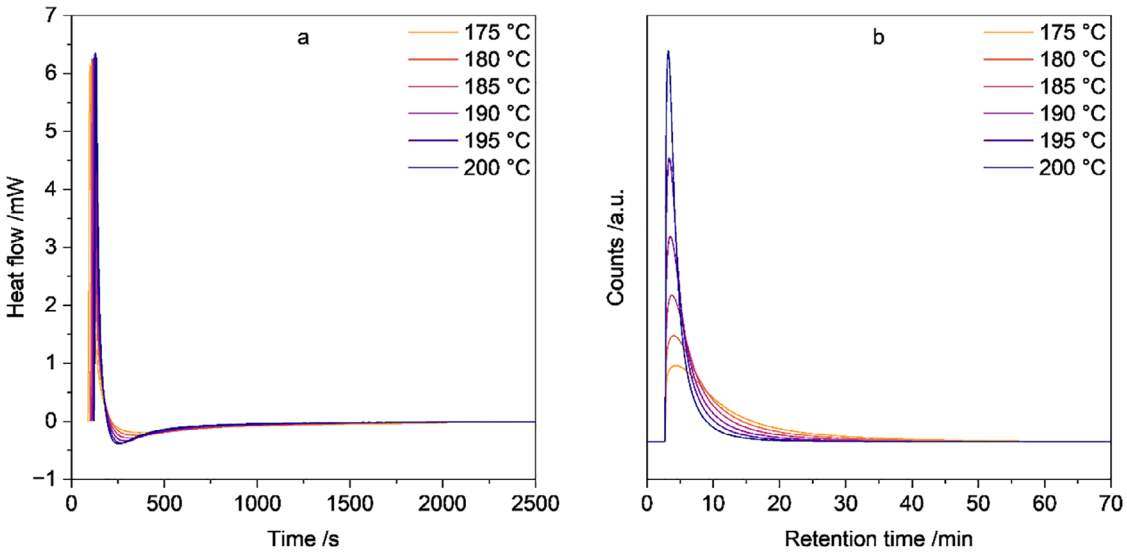

FIGURE 16 | Calorimetric (a) and FID (b) signals as a function of temperature obtained after isopropanol injection on niobium oxide.

a yield of 0.04%$_{ACE}$. It is worth mentioning that, in the same temperature range, the homogeneous conversion of isopropanol observable in an empty reactor also varies between 1 and 3%$_{PEN}$, respectively. It is very likely that the reaction occurs directly in the physisorbed layer or in the gas phase when magnesium oxide is used. Figure S16 compares the isopropanol conversion rate obtained during steady state experiments using magnesium oxide or silicium carbide (an inert material). The similar conversions obtained at the studied temperature range support the idea of a homogeneous reaction occurring with magnesium oxide. Figure 18 displays the dependence of the effective activation energy with the extent of conversion obtained after advanced kinetic computation on the exothermic contribution.

The effective activation energy of the exothermic adsorption contribution remains constant over the overall conversion range with values of 6 and 9 kJ mol^{-1} for alumina and niobium oxide, respectively. It is worth to recall that the He carrier gas flow in the calorimeter is only 30 mL min^{-1} (average linear velocity = 2.5 cm s^{-1}). Due to extremely slight variations in the shape of the exothermic peaks in the case of MgO, measurements uncertainty does not allow the effective activation energy to be accurately calculated on the overall extent of conversion. Nevertheless, at α = 50%, a value of approximately 7 kJ mol^{-1} is calculated, while at the exothermic peak maximum, values of 4 to 5 kJ mol^{-1} are obtained. The absence of variation with Al_2O_3 and Nb_2O_5 indicates that a single mechanism dominates in this temperature range. The calculated activation energies are sufficiently low not to be mistaken with important chemical reactions and are usually attributed to physical phenomena such as diffusion [79]. However, these values, although low, may correspond to the dissociation of the O—H bond of the

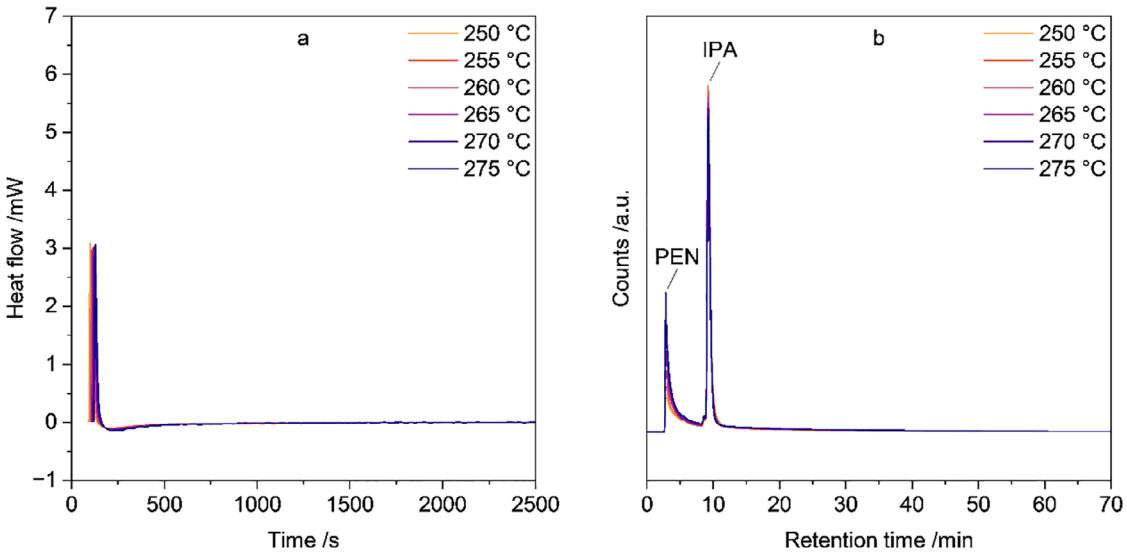

FIGURE 17 | Calorimetric (a) and FID (b) signals as a function of temperature obtained after isopropanol injection on magnesium oxide.

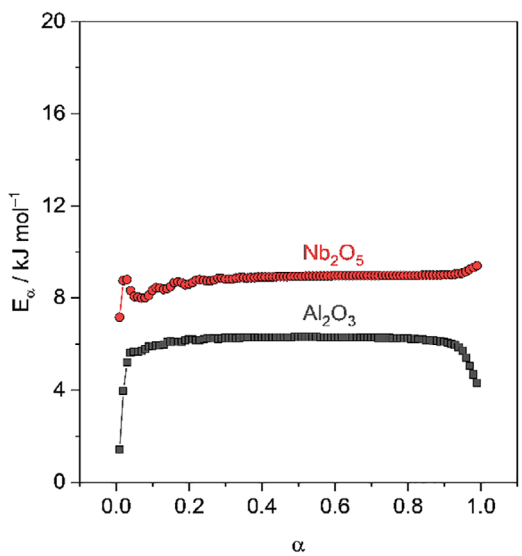

FIGURE 18 | Dependence of the effective activation energy (E_α) with extent of conversion (α) in the exhaustive adsorption contribution for alumina (square, solid, grey) and niobium oxide (circle, dash, red).

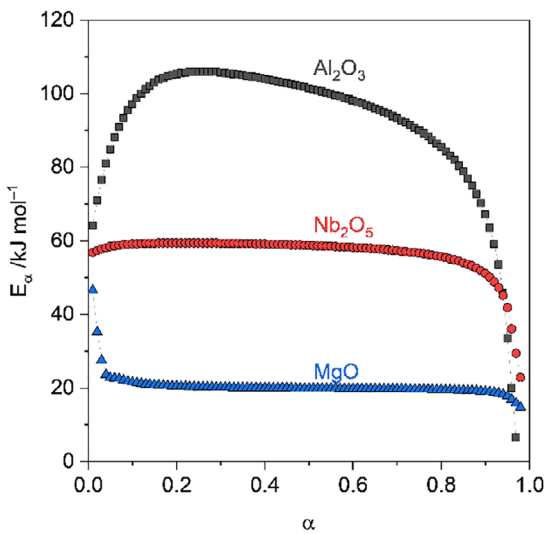

FIGURE 19 | Dependence of the effective activation energy (E_α) with extent of conversion (α) in the endothermic reaction/desorption contribution for alumina (square, solid, grey), niobium oxide (circle, dash, red) and magnesium oxide (triangle, dot, blue).

alcohol [80]. This hypothesis would explain the lower activation energy observable on alumina compared to niobium oxide, as the presence of basic sites, capable of binding protons, would allow to lower the energetic barrier for the dissociation of alcohol. Figure 19 displays the dependence of the effective activation energy with the extent of conversion obtained after advanced kinetic computation on the endothermic contribution.

The effective activation energy on alumina increases from 60 to 106 kJ mol^{-1} as the extent of conversion rises to 25%. It then decreases almost linearly to 85 kJ mol^{-1} until the conversion level reaches 80%. At this point, values quickly drop to very low levels close to 0. Niobium oxide shows a constant effective activation energy of 59 kJ mol^{-1} with a sharp decline to 23 kJ mol^{-1} when the conversion extent exceeds 90%. Magnesium oxide undergoes a dramatic decrease in activation energy during the initial 5%, dropping from 46 to 20 kJ mol^{-1}. The activation energy remains constant up to 95% conversion, at which point a subtle decrease is observed.

In all three cases, the effective activation energy at the initial stage of the catalytic process appears to be identical with a mean value of 55 kJ mol^{-1}. The rapid decrease in activation energy when the extent of conversion reaches 100%, also observable on all three catalysts, is characteristic of a diffusional regime [31, 81, 82]. This behaviour was expected as, at high extent of conversion, there is no more IPA molecules to convert. Therefore, the measured heats are only linked to desorption and diffusion of the products in the catalytic bed.

The constant activation energy found in niobium oxide until the extent of conversion of 90% suggests that a single step is predominantly rate-limiting. This value aligns with those observed during the initial stage of the two other samples and is believed to correspond to a common step in each catalytic mechanism. This effective activation energy is similar to the one obtained in a previous study, and attributed to the C—O bond cleavage during an $E1_{cb}$ mechanism [31]. However, an $E1_{cb}$ reaction is unlikely on niobium oxide, as it requires basic sites to form the carbanion intermediate by the abstraction of the hydrogen in β position of the alcohol function. Instead, an E1 pathway involving the formation of a carbocation is more likely. The presence of Brønsted acid sites, as concluded by the ammonia infrared adsorption experiment, supports this hypothesis, since Brønsted acid sites favour this mechanism and would be generated by the reaction water [7, 14].

The effective activation energy measured with magnesium oxide between the extent of conversion of 10% to 90% is too low to be associated with a chemical reaction. In this case, the conversion of IPA to PEN is too low (1% to 3%) and the reaction heat is not significant in the overall thermal increment. Therefore, the device only measures the heats of adsorption, desorption and diffusion through the catalytic bed of isopropanol. This interpretation supports the idea that adsorption on the catalyst is not strong enough to induce a surface reaction. Instead, the homogeneous reaction takes place in the gas phase.

The large variation in effective activation energy on the alumina sample suggests either (i) a mechanism in which the rate-limiting step is a function of the catalytic process, or (ii) the coexistence of two distinct mechanisms. The value obtained at 25% conversion is comparable to those obtained in conventional steady-state experiments and is often attributed to an E2 mechanism [14]. In both ways, the values are comparable to that obtained using density function theory [80]. It is likely that the variation and potential shift of the predominant mechanism on alumina is a consequence of the water produced during the reaction. As shown previously (Figure 8), the large impact of surface hydroxyls on isopropanol adsorption and the presence of new surface hydroxyls at define temperatures can argue for punctual surface modifications. This would explain the brutal shift of effective activation energy on the first 25% of conversion extent as the water produced modifies the active sites nature and strength for subsequent surface reactions in the catalytic bed.

To support this hypothesis, another amphoteric oxide was tested in isopropanol dehydration reaction. An amorphous silica–alumina sample (with a $SiO_2/(SiO_2 + Al_2O_3)$ ratio of 30%) was chosen as silica–alumina catalysts shown to be promising for alcohol dehydration [83–86]. The characterisation of the nature, strength and distribution of the acid–base sites of this sample is available in a previous study [60]. Compared to alumina, silica–alumina displays lower surface densities of acid and basic sites, which is the expected behaviour, as pure silica does not show significant acidic or basic behaviour compared to alumina [14, 87]. However, the modification of alumina with silica could induce the formation of bridged hydroxy groups, as displayed by zeolites, and modify the nature of the overall acid sites nature [88]. Figure 20 displays the calorimetric and FID signals obtained after isopropanol injection at different temperatures between 125°C and 175°C for the silica–alumina.

Like alumina and niobium oxide, isopropanol complete conversion to propylene was observed. However, significant variation in the shape of the endothermic calorimetric signal (Figure 20a) and propylene FID peak (Figure 20b) are observed at lower temperatures (125 to 150°C) for silica–alumina than for alumina, which showed the same behaviour between 150°C and 175°C, and even at a higher temperature for niobium oxide (between 175°C and 200°C). This shift to lower temperatures is indicative of an improvement in the catalytic activity compared to pure alumina. The isopropanol pulse calorimetry allowed to discriminate the temperature interval where the catalyst becomes active. Figure 21 displays the dependence of the effective activation energy with the extent of conversion obtained after advanced kinetic computation on the endothermic contribution.

On silica–alumina, the initial effective activation energy increases from 72 to 86 kJ mol^{-1} as the extent of conversion reaches 17%. The value then decreases to 45 kJ mol^{-1} up to an extent of 80%. Above this point, the effective activation energy decreases rapidly to very low values. The effective activation energy over the extent of conversion displays a similar profile as alumina but with lower values of effective activation energy. Both catalysts show an increase in the very first steps of the conversion, followed by a relatively low decrease, up to approximately 80% to 90% of α. The comparable patterns of the effective activation energy as a function of the extent of conversion observed with alumina and silica–alumina samples suggest that they share a similar mechanistic behaviour.

4 | Conclusions

The impact of the acid–base sites nature, strength and distribution on the catalytic dehydration mechanism of isopropanol to propylene and water was investigated using data from static adsorption calorimetry, in situ pulse flow calorimetry, infrared experiments and advanced kinetic computations. Alumina, niobium oxide and magnesium oxide were studied as amphoteric, acidic and basic solids, respectively. Acid sites have shown to be essential to coordinatively adsorb isopropanol under pulse catalytic testing and to trigger the dehydration surface reaction. Basic sites alone showed only physical adsorption of isopropanol under a continuous inert flow and no significant catalytic activity even at elevated temperatures. However, when associated with acidic sites in amphoteric oxides, basic sites enhance reactivity by promoting alcohol dissociation and alkoxide formation. Kinetic computations revealed that the surface mechanism is a function of active sites configuration. Both E1cb and E2 pathways were observed for isopropanol conversion on amphoteric catalysts depending on the presence of water formed during the reaction. Acid catalysts favoured isopropanol dehydration through E1 elimination and carbocation stabilisation. This study underscores the role of acid–base sites in the catalytic dehydration of isopropanol and provides a framework for tunning the surface acid–base properties in order to enhance the catalysts activity.

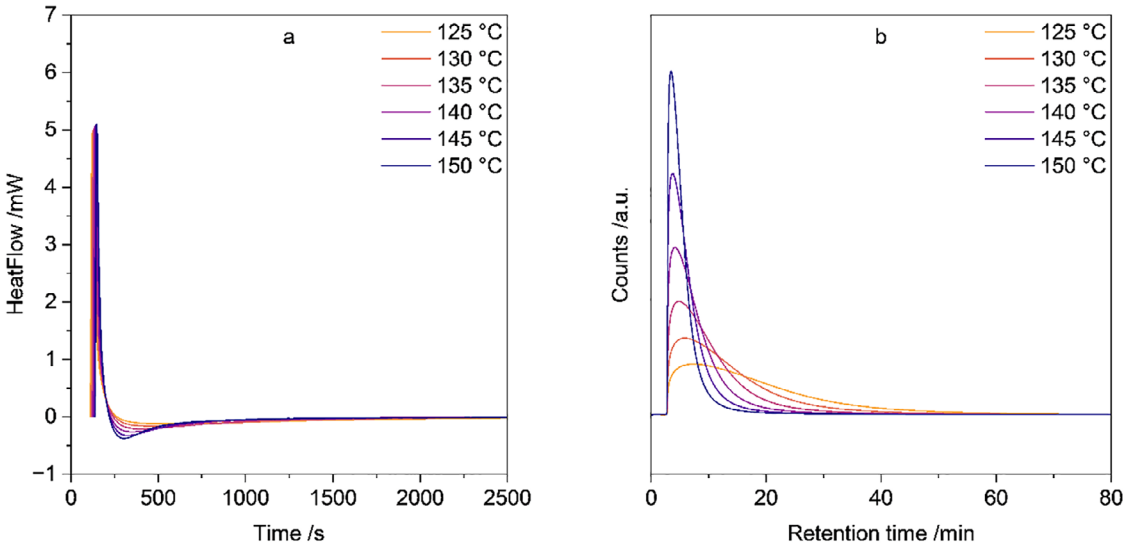

FIGURE 20 | Calorimetric (a) and FID (b) signals as a function of temperature obtained after isopropanol injection on silica–alumina.

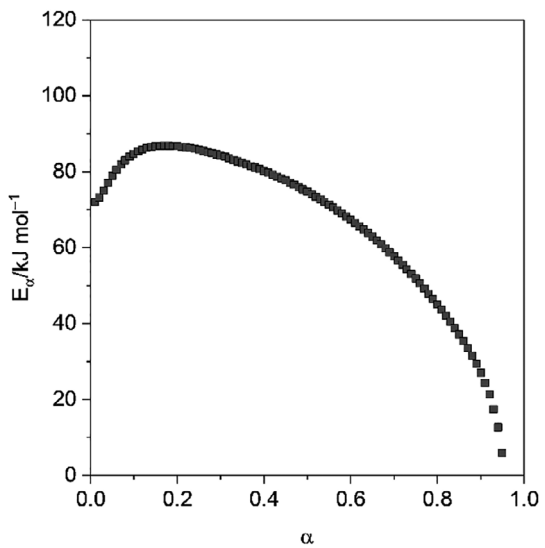

FIGURE 21 | Dependence of the effective activation energy (E_α) with extent of conversion (α) in the endothermic reaction/desorption contribution for silica–alumina.

Author Contributions

Tristan Cabanis: writing – original draft, visualisation, software, methodology, investigation and formal analysis. **Aline Auroux**: writing – review and editing, conceptualisation and validation. **Jean-Luc Dubois**: writing – review and editing and validation. **Nicolas Sbirrazzuoli**: writing – review and editing, software, formal analysis and validation. **Georgeta Postole**: writing – review and editing, supervision, project administration, methodology, conceptualisation and validation.

Acknowledgments

This work is a part of PYROCO2 project that has received funding from the European Union's Horizon 2020 research and innovation program under grant agreement no. 101037009. Tristan Cabanis thanks Tien-Hoan Nguyen for valuable technical contribution to acid–base characterisation.

Conflicts of Interest

The authors declare no conflicts of interest.

Data Availability Statement

The data that support the findings of this study are available from the corresponding author upon reasonable request.

References

1. T. K. Phung, T. L. M. Pham, K. B. Vu, and G. Busca, "(Bio)Propylene Production Processes: A Critical Review," *Journal of Environmental Chemical Engineering* 9 (2021): 105673, https://doi.org/10.1016/j.jece.2021.105673.

2. Statista, "Propylene Production Capacity Globally 2018-2030," can be found under https://www.statista.com/statistics/1065879/global-propylene-production-capacity/, 2024 (accessed 17 December 2025).

3. H. Zimmermann in *Ullmann's Encyclopedia of Industrial Chemistry* (John Wiley & Sons, Ltd, 2013), https://doi.org/10.1002/14356007.a22_211.pub3.

4. A. Corma, F. V. Melo, L. Sauvanaud, and F. Ortega, "Light Cracked Naphtha Processing: Controlling Chemistry for Maximum Propylene Production," *Catalysis Today* 107–108 (2005): 699–706, https://doi.org/10.1016/j.cattod.2005.07.109.

5. V. Blay, E. Epelde, R. Miravalles, and L. A. Perea, "Converting Olefins to Propene: Ethene to Propene and Olefin Cracking," *Catalysis Reviews* 60 (2018): 278–335, https://doi.org/10.1080/01614940.2018.1432017.

6. A. V. Lavrenov, L. F. Saifulina, E. A. Buluchevskii, and E. N. Bogdanets, "Propylene Production Technology: Today and Tomorrow," *Catalysis in Industry* 7 (2015): 175–187, https://doi.org/10.1134/S2070050415030083.

7. J.-L. Dubois, G. Postole, L. Silvester, and A. Auroux, "Catalytic Dehydration of Isopropanol to Propylene," *Catalysts* 12 (2022): 1097, https://doi.org/10.3390/catal12101097.

8. S. Basu and N. C. Pradhan, "Kinetics of Acetone Hydrogenation for Synthesis of Isopropyl Alcohol Over Cu-Al Mixed Oxide Catalysts," *Catalysis Today* 348 (2020): 118–126, https://doi.org/10.1016/j.cattod.2019.07.051.

9. V. M. Zakoshansky, "The Cumene Process for Phenol-Acetone Production," *Petroleum Chemistry* 47 (2007): 273–284, https://doi.org/10.1134/S096554410704007X.

10. K. Sale, "Shift in MMA Production Methods Threatens Acetone Consumption," can be found under https://www.icis.com/explore/resources/news/2018/06/07/10229537/shift-in-mma-production-methods-threatens-acetone-consumption, 2018 (accessed 29 December 2025).

11. A. Greenwood, "Mitsubishi's Proposed US MMA Plant Reaches Regulatory Milestones," can be found under https://www.icis.com/explore/resources/news/2024/02/06/10969428/mitsubishi-s-proposed-us-mma-plant-reaches-regulatory-milestones, 2024 (accessed 29 December 2025).

12. Y. Yue, B. Wang, A. Wang, et al., "Sustainable Catalytic Strategies for Methyl Methacrylate Synthesis: Mechanistic-Guided Design of High-Efficiency Catalysts," *Materials Today Chemistry* 46 (2025): 102746, https://doi.org/10.1016/j.mtchem.2025.102746.

13. A. Ouqour, G. Coudurier, and J. C. Vedrine, "Acid–Base Properties of Metallic Oxide Catalysts Studied by Conversion of Propan-2-ol," *Journal of the Chemical Society, Faraday Transactions* 89 (1993): 3151–3155, https://doi.org/10.1039/FT9938903151.

14. A. Gervasini, J. Fenyvesi, and A. Auroux, "Study of the Acidic Character of Modified Metal Oxide Surfaces Using the Test of Isopropanol Decomposition," *Catalysis Letters* 43 (1997): 219–228, https://doi.org/10.1023/A:1018979731407.

15. W. Turek, J. Haber, and A. Krowiak, "Dehydration of Isopropyl Alcohol Used as an Indicator of the Type and Strength of Catalyst Acid Centres," *Applied Surface Science* 252 (2005): 823–827, https://doi.org/10.1016/j.apsusc.2005.02.059.

16. C. Lahousse, J. Bachelier, J.-C. Lavalley, H. Lauron-Pernot, and A.-M. Le Govic, "Validity of Using Isopropanol Decomposition as a Test-Reaction for the Characterization of Metal Oxides Basicity; Comparison With Results Obtained From Methylbutynol Decomposition," *Journal of Molecular Catalysis* 87 (1994): 329–332, https://doi.org/10.1016/0304-5102(93)E0232-6.

17. M. Guisnet and L. Pinard, "Characterization of Acid-Base Catalysts Through Model Reactions," *Catalysis Reviews* 60 (2018): 337–436, https://doi.org/10.1080/01614940.2018.1446683.

18. H. Lauron-Pernot, "Evaluation of Surface Acido-Basic Properties of Inorganic-Based Solids by Model Catalytic Alcohol Reaction Networks," *Catalysis Reviews* 48 (2006): 315–361, https://doi.org/10.1080/01614940600816634.

19. A. Auroux and A. Gervasini, "Microcalorimetric Study of the Acidity and Basicity of Metal Oxide Surfaces," *Journal of Physical Chemistry* 94 (1990): 6371–6379, https://doi.org/10.1021/j100379a041.

20. G. Busca, "The Surface Acidity of Solid Oxides and Its Characterization by IR Spectroscopic Methods. An Attempt at Systematization," *Physical Chemistry Chemical Physics* 1 (1999): 723–736, https://doi.org/10.1039/a808366e.

21. C. Morterra and G. Magnacca, "A Case Study: Surface Chemistry and Surface Structure of Catalytic Aluminas, as Studied by Vibrational Spectroscopy of Adsorbed Species," *Catalysis Today* 27 (1996): 497–532, https://doi.org/10.1016/0920-5861(95)00163-8.

22. A. Auroux, *Acidity and Basicity* (Springer, 2006): 45–152, https://doi.org/10.1007/3829_008.

23. P. Le Parlouër, *in Calorimetry and Thermal Methods in Catalysis*, ed. A. Auroux, (Springer, 2013): 51–101, https://doi.org/10.1007/978-3-642-11954-5_2.

24. J. Xu, Q. Wang, S. Li, and F. Deng, in *Solid-State NMR in Zeolite Catalysis*, eds. J. Xu, Q. Wang, S. Li, and F. Den, (Springer, 2019): 159–197, https://doi.org/10.1007/978-981-13-6967-4_5.

25. R. J. Cvetanović and Y. Amenomiya, in *Advances in Catalysis*, (Elsevier, 1967): 103–149, https://doi.org/10.1016/S0360-0564(08)60686-0.

26. L. Damjanović and A. Auroux, in *Zeolite Chemistry and Catalysis*, eds A.W. Chester, E.G. Derouan, (Springer Netherlands, 2009): 107–167, https://doi.org/10.1007/978-1-4020-9678-5_3.

27. J. C. Védrine, "Acid–Base Characterization of Heterogeneous Catalysts: An Up-To-Date Overview," *Research on Chemical Intermediates* 41 (2015): 9387–9423, https://doi.org/10.1007/s11164-015-1982-9.

28. V. Morávek, M. Kraus, L. V. Malysheva, E. A. Paukshtis, and E. N. Yurchenko, "IR study of Dynamic Bahaviour of 2-Propanol on Alumina," *Collection of Czechoslovak Chemical Communications* 53 (1988): 459–465, https://doi.org/10.1135/cccc19880459.

29. E. Decanio, "Identification of Alcohol Adsorption Sites on γ-Alumina," *Journal of Catalysis* 135 (1992): 444–457, https://doi.org/10.1016/0021-9517(92)90046-K.

30. J. H. Kwak, D. Mei, C. H. F. Peden, R. Rousseau, and J. Szanyi, "(100) Facets of γ-Al_2O_3: The Active Surfaces for Alcohol Dehydration Reactions," *Catalysis Letters* 141 (2011): 649–655, https://doi.org/10.1007/s10562-010-0496-8.

31. T. Cabanis, A. Auroux, J.-L. Dubois, N. Sbirrazzuoli, and G. Postole, "An Innovative Approach to Evidence Pathways in a Reactional Mechanism of Heterogenous Catalysis," *Applied Catalysis O: Open* 208 (2025): 207073, https://doi.org/10.1016/j.apcato.2025.207073.

32. S. Vyazovkin, A. K. Burnham, J. M. Criado, L. A. Pérez-Maqueda, C. Popescu, and N. Sbirrazzuoli, "ICTAC Kinetics Committee Recommendations for Performing Kinetic Computations on Thermal Analysis Data," *Thermochimica Acta* 520 (2011): 1–19, https://doi.org/10.1016/j.tca.2011.03.034.

33. S. Vyazovkin, K. Chrissafis, M. L. Di Lorenzo, et al., "ICTAC Kinetics Committee Recommendations for Collecting Experimental Thermal Analysis Data for Kinetic Computations," *Thermochimica Acta* 590 (2014): 1–23, https://doi.org/10.1016/j.tca.2014.05.036.

34. S. Vyazovkin, A. K. Burnham, L. Favergeon, et al., "ICTAC Kinetics Committee Recommendations for Analysis of Multi-Step Kinetics," *Thermochimica Acta* 689 (2020): 178597, https://doi.org/10.1016/j.tca.2020.178597.

35. N. Sbirrazzuoli, "Determination of Pre-Exponential Factors and of the Mathematical Functions f(α) or G(α) That Describe the Reaction Mechanism in a Model-Free Way," *Thermochimica Acta* 564 (2013): 59–69, https://doi.org/10.1016/j.tca.2013.04.015.

36. N. Sbirrazzuoli, "Determination of Pre-Exponential Factor and Reaction Mechanism in a Model-Free Way," *Thermochimica Acta* 691 (2020): 178707, https://doi.org/10.1016/j.tca.2020.178707.

37. N. Sbirrazzuoli, "Advanced Isoconversional Kinetic Analysis: Insight in Mechanisms and Simulations. Successes and Future," *Thermochimica Acta* 733 (2024): 179688, https://doi.org/10.1016/j.tca.2024.179688.

38. S. N. Kabekkodu, A. Dosen, and T. N. Blanton, "PDF-5+: A comprehensive Powder Diffraction File™ for Materials Characterization," *Powder Diffraction* 39 (2024): 47–59, https://doi.org/10.1017/S0885715624000150.

39. T. Horikawa, D. D. Do, and D. Nicholson, "Capillary Condensation of Adsorbates in Porous Materials," *Advances in Colloid and Interface Science* 169 (2011): 40–58, https://doi.org/10.1016/j.cis.2011.08.003.

40. K. S. W. Sing, "Reporting Physisorption Data for Gas/Solid Systems With Special Reference to the Determination of Surface Area and Porosity (Recommendations 1984)," *Pure and Applied Chemistry* 57 (1985): 603–619, https://doi.org/10.1351/pac198557040603.

41. A. L. F. Dullien in *Porous Media* (Elsevier, 1992): 117–236, https://doi.org/10.1016/B978-0-12-223651-8.50008-0.

42. F. Rouquerol, J. Rouquerol, and K. Sing, in *Adsorption by Powders and Porous Solids*, (Elsevier, 1999): 439–447, https://doi.org/10.1016/B978-012598920-6/50014-2.

43. D. H. Everett and F. S. Stone, *The Structure and Properties of Porous Materials* (Butterworths,1958).

44. J. Deboer, "Studies on Pore Systems in Catalysts II. The Shapes of Pores in Aluminum Oxide Systems," *Journal of Catalysis* 3 (1964): 38–43, https://doi.org/10.1016/0021-9517(64)90090-9.

45. M. Thommes, "Physical Adsorption Characterization of Nanoporous Materials," *Chemie Ingenieur Technik* 82 (2010): 1059–1073, https://doi.org/10.1002/cite.201000064.

46. L. R. V. Da Conceição, L. M. Carneiro, J. D. Rivaldi, and H. F. De Castro, "Solid Acid as Catalyst for Biodiesel Production via Simultaneous Esterification and Transesterification of Macaw Palm Oil," *Industrial Crops and Products* 89 (2016): 416–424, https://doi.org/10.1016/j.indcrop.2016.05.044.

47. S. A. Fuente, C. A. Ferretti, N. F. Domancich, et al., "Adsorption of 2-Propanol on MgO Surface: A Combined Experimental and Theoretical Study," *Applied Surface Science* 327 (2015): 268–276, https://doi.org/10.1016/j.apsusc.2014.11.159.

48. C. Chizallet, G. Costentin, M. Che, F. Delbecq, and P. Sautet, "Infrared Characterization of Hydroxyl Groups on MgO: A Periodic and Cluster Density Functional Theory Study," *Journal of the American Chemical Society* 129 (2007): 6442–6452, https://doi.org/10.1021/ja068720e.

49. G. Szöllösi and M. Bartók, "Hydrogenation of Unsaturated Ketones: Selective Catalytic Transfer Hydrogenation of 5-Hexen-2-one Over MgO," *Journal of Molecular Catalysis A: Chemical* 148 (1999): 265–273, https://doi.org/10.1016/S1381-1169(99)00159-4.

50. H. Knözinger and P. Ratnasamy, "Catalytic Aluminas: Surface Models and Characterization of Surface Sites," *Catalysis Reviews* 17 (1978): 31–70, https://doi.org/10.1080/03602457808080878.

51. H. K. Knözinger, in *Studies in Surface Science and Catalysis*, (Elsevier, 1985): 111–125, https://doi.org/10.1016/S0167-2991(09)60161-0.

52. G. Busca, "The Surface of Transitional Aluminas: A Critical Review," *Catalysis Today* 226 (2014): 2–13, https://doi.org/10.1016/j.cattod.2013.08.003.

53. J. V. Evans and T. L. Whateley, "Infra-Red Study of Adsorption of Carbon Dioxide and Water on Magnesium Oxide," *Transactions of the Faraday Society* 63 (1967): 2769–2777, https://doi.org/10.1039/tf9676302769.

54. R. Philipp and K. Fujimoto, "FTIR Spectroscopic Study of Carbon Dioxide Adsorption/Desorption on Magnesia/Calcium Oxide Catalysts," *Journal of Physical Chemistry* 96 (1992): 9035–9038, https://doi.org/10.1021/j100201a063.

55. J. Szanyi and J. H. Kwak, "Dissecting the Steps of CO_2 reduction: 1. The interaction of CO and CO_2 With γ-Al_2O_3: An In Situ FTIR study," *Physical Chemistry Chemical Physics* 16 (2014): 15117–15125, https://doi.org/10.1039/C4CP00616J.

56. C. Gómez and J. Rodríguez-Páez, "The Effect of the Synthesis Conditions on Structure and Photocatalytic Activity of Nb_2O_5 Nanostructures," *Processing and Application of Ceramics* 12 (2018): 218–229, https://doi.org/10.2298/PAC1803218G.

57. E. P. L. Hunter and S. G. Lias, "Evaluated Gas Phase Basicities and Proton Affinities of Molecules: An Update," *Journal of Physical and Chemical Reference Data* 27 (1998): 413–656, https://doi.org/10.1063/1.556018.

58. D. W. Breck, *Zeolite Molecular Sieves: Structure, Chemistry, and Use* (Wiley, 1974), https://doi.org/10.1093/chromsci/13.4.18A-c.

59. A. Gervasini and A. Auroux, "Thermodynamics of Adsorbed Molecules for a New Acid-Base Topochemistry of Alumina," *Journal of Physical Chemistry* 97 (1993): 2628–2639, https://doi.org/10.1021/j100113a026.

60. G. Postole, S. Segondy, T. Cabanis, T.-H. Nguyen, A. Auroux, and J.-L. Dubois, "Relationship Between Number and Strength of Acid–Base Catalytic Sites and Their Performances in Isopropanol Dehydration Reaction," *Catalysts* 15 (2025): 768, https://doi.org/10.3390/catal15080768.

61. J. B. Peri, "Infrared Study of Adsorption of Ammonia on Dry γ-Alumina[1]," *Journal of Physical Chemistry A* 69 (1965): 231–239, https://doi.org/10.1021/j100885a034.

62. D. Stoilova, K. Cheshkova, and R. Nickolov, "FTIR Spectroscopy of NH^3 and NO Adsorption on Copper-on-Alumina Catalysts," *Reaction Kinetics and Catalysis Letters* 68 (1999): 331–337, https://doi.org/10.1007/BF02475521.

63. K. T. Cheshkova and D. G. Stoilova, "FTIR Spectroscopic Study of NH3 and NH3 Adsorption on Alumina-Supported Mixed Copper-Manganese Oxide Catalysts," *Reaction Kinetics and Catalysis Letters* 73 (2001): 237–243, https://doi.org/10.1023/A:1014190703421.

64. G. F. Svatos, D. M. Sweeny, S.-I. Mizushima, C. Curran, and J. V. Quagliano, "Infrared Absorption Spectra of Inorganic Coördination Complexes.[1a,b] XII. The Characteristic NH_3 Deformation Vibrations of Solid Inorganic Complexes.[1a,b] XII. The Characteristic NH_3 Deformation Vibrations of Solid Inorganic Complexes," *Journal of the American Chemical Society* 79 (1957): 3313–3315, https://doi.org/10.1021/ja01570a004.

65. M. Paulis, M. Martıń, D. B. Soria, A. Dıáz, J. A. Odriozola, and M. Montes, "Preparation and Characterization of Niobium Oxide for the Catalytic Aldol Condensation of Acetone," *Applied Catalysis A: General* 180 (1999): 411–420, https://doi.org/10.1016/S0926-860X(98)00379-2.

66. S. Coluccia, S. Lavagnino, and L. Marchese, "Adsorption and Dissociation of Ammonia on the Hydroxylated Surface of Magnesium Oxide Powders," *Journal of the Chemical Society, Faraday Transactions 1: Physical Chemistry in Condensed Phases* 83 (1987): 477–486, https://doi.org/10.1039/f19878300477.

67. A. V. Deo, T.-T. Chuang, and I. G. Dalla Lana, "Infrared Studies of Adsorption and Surface Reactions of Some Secondary Alcohols, C3 to C5, on .Gamma.-Alumina and .Gamma.-Alumina Doped With Sodium Hydroxide," *Journal of Physical Chemistry* 75 (1971): 234–239, https://doi.org/10.1021/j100672a009.

68. R. O. Kagel, "Infrared Investigation of the Adsorption and Surface Reactions of the C1 Through C4 Normal Alcohols on γ-Alumina," *Journal of Physical Chemistry* 71 (1967): 844–850, https://doi.org/10.1021/j100863a010.

69. R. G. Greenler, "Infrared Study of the Adsorption of Methanol and Ethanol on Aluminum Oxide," *Journal of Chemical Physics* 37 (1962): 2094–2100, https://doi.org/10.1063/1.1733430.

70. J. E. Bertie, M. K. Ahmed, and H. H. Eysel, "Infrared Intensities of Liquids. 5. Optical and Dielectric Constants, Integrated Intensities, and Dipole Moment Derivatives of Water and Water-d2 at 22.degree.C. Optical and Dielectric Constants, Integrated Intensities, and Dipole Moment Derivatives of H_2O and D_2O at 22°C," *Journal of Physical Chemistry* 93 (1989): 2210–2218, https://doi.org/10.1021/j100343a008.

71. H. A. Al-Abadleh and V. H. Grassian, "FT-IR Study of Water Adsorption on Aluminum Oxide Surfaces," *Langmuir* 19 (2003): 341–347, https://doi.org/10.1021/la026208a.

72. J. Jain, "Catalytic Dehydration of Alcohols Over Alumina Mechanism of Ether Formation," *Journal of Catalysis* 9 (1967): 322–330, https://doi.org/10.1016/0021-9517(67)90260-6.

73. J. I. Di Cosimo, V. K. Dıéz, M. Xu, E. Iglesia, and C. R. Apesteguıá, "Structure and Surface and Catalytic Properties of Mg-Al Basic Oxides," *Journal of Catalysis* 178 (1998): 499–510, https://doi.org/10.1006/jcat.1998.2161.

74. S. Ito, X. Wang, A. Waheed, et al., "Support Effects in Iridium-Catalyzed Aerobic Oxidation of Benzyl Alcohol Studied by Modulation-Excitation Attenuated Total Reflection IR Spectroscopy," *Journal of Catalysis* 393 (2021): 42–50, https://doi.org/10.1016/j.jcat.2020.11.010.

75. B. Fubini, V. Bolis, M. Bailes, and F. Stone, "The Reactivity of Oxides With Water Vapor," *Solid State Ionics* 32-33 (1989): 258–272, https://doi.org/10.1016/0167-2738(89)90230-0.

76. J. G. Speight, ed., *Lange's Handbook of Chemistry*, 17th ed, (McGraw-Hill, 2021).

77. M. E. Van Leeuwen, "Derivation of Stockmayer Potential Parameters for Polar Fluids," *Fluid Phase Equilibria* 99 (1994): 1–18, https://doi.org/10.1016/0378-3812(94)80018-9.

78. C. W. Bale, E. Bélisle, P. Chartrand, et al., "FactSage Thermochemical Software and Databases, 2010–2016," *Calphad* 54 (2016): 35–53, https://doi.org/10.1016/j.calphad.2016.05.002.

79. S. Vyazovkin, *Isoconversional Kinetics of Thermally Stimulated Processes* (Springer International Publishing, 2015), https://doi.org/10.1007/978-3-319-14175-6.

80. K. Larmier, C. Chizallet, N. Cadran, et al., "Mechanistic Investigation of Isopropanol Conversion on Alumina Catalysts: Location of Active Sites for Alkene/Ether Production," *ACS Catalysis* 5 (2015): 4423–4437, https://doi.org/10.1021/acscatal.5b00723.

81. S. Vyazovkin and N. Sbirrazzuoli, "Mechanism and Kinetics of Epoxy–Amine Cure Studied by Differential Scanning Calorimetry," *Macromolecules* 29 (1996): 1867–1873, https://doi.org/10.1021/ma951162w.

82. N. Sbirrazzuoli, "Interpretation and Physical Meaning of Kinetic Parameters Obtained From Isoconversional Kinetic Analysis of Polymers," *Polymers* 12 (2020): 1280, https://doi.org/10.3390/polym12061280.

83. G. Busca, "Catalytic Materials Based on Silica and Alumina: Structural Features and Generation of Surface Acidity," *Progress in Materials Science* 104 (2019): 215–249, https://doi.org/10.1016/j.pmatsci.2019.04.003.

84. T. K. Phung and G. Busca, "Ethanol Dehydration on Silica-Aluminas: Active Sites and Ethylene/Diethyl Ether Selectivities," *Catalysis Communications* 68 (2015): 110–115, https://doi.org/10.1016/j.catcom.2015.05.009.

85. C. Chizallet and P. Raybaud, "Pseudo-Bridging Silanols as Versatile Brønsted Acid Sites of Amorphous Aluminosilicate Surfaces," *Angewandte Chemie* 121 (2009): 2935–2937, https://doi.org/10.1002/ange.200804580.

86. K. Larmier, C. Chizallet, S. Maury, et al., "Isopropanol Dehydration on Amorphous Silica–Alumina: Synergy of Brønsted and Lewis Acidities at Pseudo-Bridging Silanols," *Angewandte Chemie International Edition* 56 (2017): 230–234, https://doi.org/10.1002/anie.201609494.

87. A. Gervasini and A. Auroux, "Acidity and Basicity of Metal Oxide Surfaces II. Determination by Catalytic Decomposition of Isopropanol," *Journal of Catalysis* 131 (1991): 190–198, https://doi.org/10.1016/0021-9517(91)90335-2.

88. W. Daniell, U. Schubert, R. Glöckler, A. Meyer, K. Noweck, and H. Knözinger, "Enhanced Surface Acidity in Mixed Alumina–Silicas: A Low-Temperature FTIR Study," *Applied Catalysis A: General* 196 (2000): 247–260, https://doi.org/10.1016/S0926-860X(99)00474-3.

Supporting Information

Additional supporting information can be found online in the Supporting Information section.

Supporting File: cctc70700-sup-0001-SuppMat.docx.